Advancing Seismic Slope Instability Monitoring: Integrating Fibre-Optic and Nodal Array Sensing

Tjeerd Kiers [ID] * [1], **Cédric Schmelzbach** [ID] [1], **Florian Amann** [ID] [2], **Hansruedi Maurer** [ID] [1], **Pascal Edme** [ID] [1], **Antonio Pio Rinaldi** [ID] [1], **Yves Bonanomi** [3], **Johan Robertsson** [ID] [1]

[1] Institute of Geophysics, ETH Zurich, Switzerland, [2] Engineering Geology and Hydrogeology, RWTH Aachen, Germany, [3] Bonanomi AG, Igis, Switzerland

Author contributions: *Conceptualization*: Tjeerd Kiers, Cédric Schmelzbach, Florian Amann, Hansruedi Maurer, Pascal Edme, Antonio Pio Rinaldi, Yves Bonanomi. *Methodology*: Tjeerd Kiers, Cédric Schmelzbach. *Data curation*: Tjeerd Kiers, Pascal Edme. *Formal Analysis*: Tjeerd Kiers, Cédric Schmelzbach. *Investigation*: Tjeerd Kiers, Cédric Schmelzbach. *Resources*: Florian Amann, Hansruedi Maurer, Antonio Pio Rinaldi, Yves Bonanomi, Johan Robertsson. *Writing - Original draft*: Tjeerd Kiers. *Writing - Review & Editing*: Cédric Schmelzbach, Hansruedi Maurer, Pascal Edme, Antonio Pio Rinaldi, Johan Robertsson. *Visualization*: Tjeerd Kiers. *Supervision*: Cédric Schmelzbach, Hansruedi Maurer, Johan Robertsson. *Project administration*: Cédric Schmelzbach, Johan Robertsson. *Funding acquisition*: Cédric Schmelzbach, Johan Robertsson.

Abstract   Slope instabilities pose serious risks to infrastructure and communities in mountainous regions. Understanding their internal structure and time-dependent dynamics is vital for effective hazard assessment and mitigation. The Cuolm da Vi instability in central Switzerland, one of the largest slow-moving instabilities in the Alps, offers an ideal setting for field-based slope instability research. We present the motivation, design, and implementation of a novel large-scale multi-sensor seismic network to study the subsurface structure and deformation dynamics of Cuolm da Vi across an unprecedented range of spatial and temporal scales: from decimetres to kilometres and milliseconds to years. The sensor network includes a hexagonal grid of more than 1000 seismic nodes primarily deployed for high-resolution 3D characterization. This temporary nodal array was complemented with a trenched 6.5 km fibre-optic configuration, which covers the most unstable parts of Cuolm da Vi using a multi-directional cable layout, suited for Distributed Acoustic and Strain Sensing measurements (DAS & DSS). Data acquisition spanned two years so far, including controlled-source experiments and continuous seismic and strain sensing campaigns. Initial data screening demonstrates the network's potential to facilitate imaging of the internal structure and monitoring of seasonal subsurface instability processes. Our study shows the feasibility of dense long-term seismic monitoring in challenging Alpine terrain using nodal and distributed fibre-optic sensing techniques, opening new opportunities for slope instability research and hazard assessment.

1   Introduction

Gravity-driven mass movements of rock, debris, and soil (i.e., landslides), are among the most destructive natural hazards globally (Hungr et al., 2014). Between 2004 and 2016, over 4800 events caused nearly 56,000 fatalities (Froude and Petley, 2018). Furthermore, landslides cause considerable economic losses estimated to reach billions of US dollars annually (Clague et al., 2012; Alimohammadlou et al., 2013; Sim et al., 2022). Projected climate change effects, such as intensified precipitation, are expected to increase both the frequency and magnitude of landslides (Patton et al., 2019; Handwerger et al., 2022; Jemec Auflič et al., 2023). Despite decades of research, many of such instabilities remain poorly understood, largely because their internal structure and long-term deformation processes are difficult to observe directly.

Landslides exhibit a wide variability in structure, dynamics, and failure mechanisms (Hungr et al., 2014). Consequently, long-term monitoring is crucial for cap-

turing their complex, often non-linear responses to external forcing, thereby advancing knowledge of both fundamental and site-specific processes, and enabling the development of effective early warning strategies (Handwerger et al., 2019; Lacroix et al., 2020). Multi-year monitoring initiatives, such as the French National Landslide Observatory (OMIV) (Malet et al., 2023) and the Hollin Hill landslide monitoring site in the UK (Uhlemann et al., 2016b), illustrate the value of such efforts. However, given the diversity of landslide types, mechanisms and scales (Hungr et al., 2014), there is a clear need to expand long-term monitoring efforts geographically.

One of the largest instabilities in the Alps is the Cuolm da Vi (CdV) slope. Located near Sedrun in the Central Swiss Alps, this deep-seated instability has an estimated unstable volume of approximately $150 \times 10^6 \, \text{m}^3$ (Amann, 2006). Field observations by Amann (2006) suggest a toppling mechanism oriented toward the south–southwest. Displacement measurements recorded for more than two decades indicate that the central part of CdV is currently moving at rates of up to 10–20 cm per year, with a pronounced seasonal acceleration between April

*Corresponding authors: tjeerd.kiers@eaps.ethz.ch   & cedric.schmelzbach@eaps.ethz.ch

and July, likely controlled by snowmelt infiltration. Despite ongoing surface monitoring and previous studies (e.g., Amann, 2006; Kleinbrod et al., 2017; Bickel et al., 2018), key questions remain regarding, for example, the vertical extent of the unstable mass and subsurface deformation processes.

Traditional landslide monitoring methods, such as borehole drilling, provide point-scale geomechanical data, but are costly and spatially limited (Corominas et al., 2000; Lee et al., 2008; Uhlemann et al., 2016b). Geodetic and remote sensing techniques, including digital image correlation and laser tachymetry, enable spatially broad and long-term monitoring (Gili et al., 2000; Rossi et al., 2016; Zhao and Lu, 2018; Shen et al., 2021). However, these methods provide surface observations only and, consequently, are inherently of limited value for studying subsurface structures, mechanical properties, and internal dynamics.

Geophysical methods address the limitations of surface observations by enabling 2D and 3D subsurface imaging in a non-invasive and cost-effective manner (Jongmans and Garambois, 2007; Malehmir et al., 2013; Whiteley et al., 2019). For example, electrical resistivity techniques have been employed to investigate internal landslide moisture dynamics (Perrone et al., 2014; Whiteley et al., 2023), while ground-penetrating radar has been used to map landslide structures (Heincke et al., 2006a; Kannaujiya et al., 2019). Seismic methods are of particular interest for the imaging and monitoring of landslides because the elastic parameters governing the propagation of seismic waves can be related to mechanical properties (Uhlemann et al., 2016a). Controlled-source seismic techniques have been used to delineate the internal structure of unstable slopes (Heincke et al., 2006b; Samyn et al., 2012; Pertuz and Malehmir, 2023). In addition, passive seismic approaches have been used to exploit signals generated by landslide-induced seismic activity (Helmstetter and Garambois, 2010; Provost et al., 2018), or variations in ambient seismic vibrations, to monitor temporal changes in subsurface structures (Mainsant et al., 2012; Le Breton et al., 2021). However, current applications of seismic techniques in landslide research and monitoring are often limited by small numbers of sensors, that can be installed with reasonable effort in the often challenging environment.

Two recent advances in seismic sensing technology offer new potential for landslide research and monitoring (Goldswain, 2020; Li, 2021). Firstly, the development of lightweight autonomous nodal seismic systems has facilitated the rapid deployment of extensive, dense seismic arrays, even in remote or challenging terrain (Hansen and Schmandt, 2015; Hudson et al., 2024; O'toole et al., 2024). Secondly, fibre-optic sensing technologies, such as Distributed Acoustic Sensing (DAS), are currently transforming seismic monitoring, by utilizing fibre-optic cables to obtain high-resolution (e.g., metre-scale), distributed seismic measurements over cable lengths of several kilometres (Ajo-Franklin et al., 2019; Lindsey and Martin, 2021). Together, these innovations offer a unique opportunity to characterize and monitor subsurface landslide dynamics with unprece-

dented resolution in space and time.

The CdV site offers the opportunity to establish a unique seismic landslide monitoring laboratory, to explore the potential and advance the use of large nodal arrays and distributed fibre optic sensing. This allows us to deepen our fundamental understanding of slope instability processes by investigating the internal structure, physical properties, and time-dependent dynamics of the CdV instability. Our unique instrumentation setup combines a temporary dense nodal seismic array (>1000 sensors) with a long-term network of several kilometres of fibre-optic cable for DAS and DSS observations. This integrated, multi-sensor network enables data acquisition across an exceptionally broad range of spatial and temporal scales, to observe ground motion from millisecond-scale seismic events to long-term displacement dynamics occurring over months.

In this paper, we provide a comprehensive overview of the CdV seismic monitoring network and outline our scientific rationale, design, and deployment strategy. We review the current state of seismic and fibre-optic landslide monitoring, detail the installation and dataset, and discuss the challenges and broader implications of deploying large-scale multi-sensor networks in alpine environments.

2 Seismic and Fibre-Optic Instability Monitoring

2.1 Characterization and Monitoring Approaches

Subsurface characterization of landslides has been accomplished through active-source seismic imaging (Jongmans et al., 2000; Heincke et al., 2006b; Samyn et al., 2012). These active seismic methods are particularly well suited for high-resolution 2D and 3D imaging, as they allow for a controlled distribution of sources and receivers. A widely applied technique is first-arrival traveltime tomography, which is used to invert P-wave traveltimes to image the subsurface velocity structure (Lanz et al., 1998; Zelt et al., 2006). Such velocity models can provide effective constraints on unstable rock masses, which typically exhibit reduced seismic velocities compared to intact bedrock (Heincke et al., 2006b; Glueer et al., 2024). While this method has been successfully employed in landslide characterization studies, many applications have been limited to 2D imaging due to the logistical challenges of deploying large source and receiver arrays in steep or remote terrain. Given the often complex 3D structure of landslides, however, achieving a 3D understanding of the internal structure can be critical for accurately assessing slope instability and estimating unstable rock volumes (Erismann and Abele, 2001; Heincke et al., 2006b; Samyn et al., 2012).

Passive seismic methods, in contrast, involve the analysis of ambient seismic vibrations and microseismic events to investigate slope dynamics. Microseismicity and tremor activity observed at various landslide sites have been linked to internal deformation processes, such as stick-slip motion along internal surfaces (Finnegan et al., 2022) and shear fracturing within

unstable rock masses (Poli, 2017; Schöpa et al., 2018). These microseismic signals have been effectively used to monitor landslides and rockfalls (Spillmann et al., 2007; Provost et al., 2018), revealing correlations between microseismic event rates and slope displacement or rockslide frequency (Spillmann et al., 2007; Helmstetter and Garambois, 2010; Tonnellier et al., 2013). Consequently, seismicity rate has been proposed as a potential indicator of landslide acceleration (Senfaute et al., 2009). Moreover, the spatial distribution of microseismic events can provide valuable insights into the location, extent, and temporal evolution of active failure zones (Schöpa et al., 2018). However, the detection of such events remains challenging due to their typically low energy and significant attenuation within weathered or fractured rock layers.

The correlation of ambient seismic vibrations, generated by both natural and anthropogenic sources, has emerged as an effective technique for monitoring landslide activity through the detection of variations in apparent surface wave velocity (Le Breton et al., 2021). This method involves cross-correlating passive seismic recordings collected at pairs of sensors to approximate the Green's function between them (Shapiro and Campillo, 2004). On the one hand, this cross-correlation information can be exploited for subsurface tomography by inverting the frequency-dependent surface wave velocities towards a S-wave velocity model (Bensen et al., 2007; Rodríguez Tribaldos and Ajo-Franklin, 2021). On the other hand, the temporal analysis of the cross-correlation coda enables the detection of subtle relative velocity variations over time, indicative of changes in the physical properties of the medium between sensors (Sens-Schönfelder and Wegler, 2006). This approach has proven effective in volcanic environments, where decreases in apparent seismic velocity have been observed prior to eruptions or following seismic events (Brenguier et al., 2008; Wegler and Sens-Schönfelder, 2007). In the context of landslide monitoring, a notable example is the detection of a 7% velocity decrease preceding a landslide in Pont-Bourquin, attributed to soil fluidization due to elevated pore water pressure (Mainsant et al., 2012). Since then, this method has been successfully applied to a range of landslides, including deep-seated instabilities, earthflows, and rockfalls, demonstrating that relative changes in seismic velocity (so-called dv/v) may act as precursors to slope failure (Voisin et al., 2016; Bontemps et al., 2020; Bertello et al., 2018).

2.2 Fibre-Optic Sensing

Fibre-optic sensing technologies, such as Distributed Acoustic Sensing (DAS) and Distributed Strain Sensing (DSS), are rapidly evolving tools that enable high-resolution strain (rate) measurements along optical fibres (e.g., Masoudi and Newson, 2016; Lu et al., 2019). DAS relies on Rayleigh backscattering at fibre impurities, allowing for dense (metre-scale) spatial sampling of relative strain-rate recordings along cables extending over tens of kilometres (Ajo-Franklin et al., 2019; Lindsey and Martin, 2021). This technique has

been widely adopted for subsurface monitoring applications, including geothermal reservoirs, volcanology and cryosphere systems (e.g., review by Lindsey and Martin, 2021). Recent advances in DAS data analysis, including the application of seismic interferometry to ambient seismic vibrations recorded by DAS systems, have further extended its use to areas such as aquifer monitoring (Rodríguez Tribaldos and Ajo-Franklin, 2021). While the fibre-optic cable deployment can require significant initial effort, first DAS studies have demonstrated considerable potential for landslide and slope stability monitoring. For instance, by leveraging the broad frequency bandwidth of DAS (Paitz et al., 2021), Ouellet et al. (2024) identified low-frequency (<1 Hz) strain signals associated with an active shallow landslide. Additionally, Kang et al. (2024) introduced a semi-supervised neural network capable of distinguishing rock slope failure signals from background noise using continuous DAS recordings.

Unlike DAS, DSS systems based on Brillouin scattering enable the measurement of absolute strain values at different scales (Masoudi and Newson, 2016; Acharya and Kogure, 2022; Hopp et al., 2022). While both techniques offer dense spatial sampling, they differ significantly in temporal resolution and spatial accuracy of the event causing the strain. DAS operates at high sampling frequencies, from several hertz up to the kilohertz range, whereas DSS data are typically sampled at much lower rates, with measurement intervals on the order of minutes. Compared to DAS, where strain is typically averaged over a certain length (the so-called gauge length, usually between 1 and 20 m depending on the interrogator), DSS can detect strain-inducing events with spatial resolutions down to tens of centimetres in Brillouin-based systems. DSS measurements are sensitive to both strain and temperature variations along the fibre, necessitating co-located temperature measurements to isolate the strain component (Acharya and Kogure, 2024). The adoption of DSS has opened new possibilities for landslide monitoring by providing accurate, spatially continuous deformation measurements, addressing the limitations of traditional point-based instruments such as inclinometers (Acharya and Kogure, 2022). Laboratory experiments have demonstrated the effectiveness of DSS in detecting soil strain and assessing slope stability under controlled conditions (Minardo et al., 2015; Schenato et al., 2017). At the field scale, one of the earliest applications was carried out by Iten et al. (2009), who deployed embedded fibre-optic cables to monitor ground displacement at the Brattas and Laret landslides. A comprehensive review of recent advancements in landslide monitoring using DSS technology is provided by Acharya and Kogure (2022).

3 The Cuolm da Vi Instability

The Cuolm da Vi (CdV) deep-seated rock slope instability is located on a south-facing slope near Sedrun in the Graubünden region of the Central Swiss Alps (Figure 1). It is one of the largest and most impressive slope instabilities in the Alps, covering an area of approximately
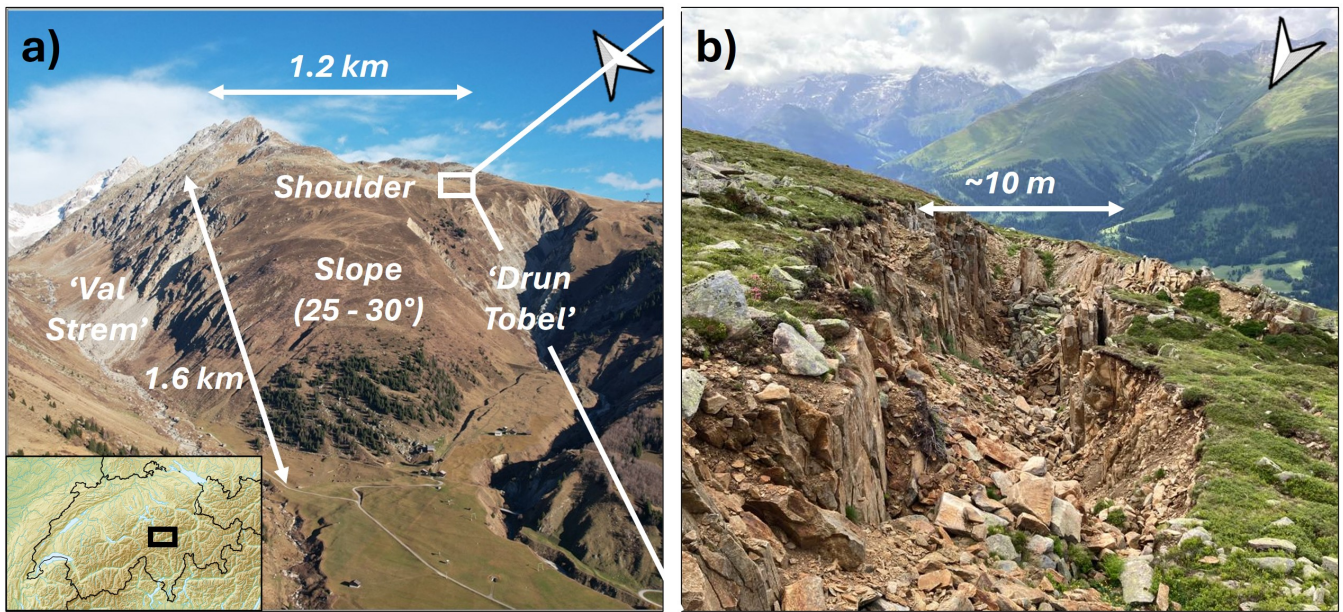
Figure 1 Overview of the Cuolm da Vi slope instability in Sedrun, Switzerland. (a) Aerial photograph of the Cuolm da Vi site captured in summer 2022, illustrating the full extent of the slope instability. (b) Close-up picture (summer 2022) of the large-scale crack marking the eastern instability boundary.

1.5 km^2 and comprising an estimated unstable volume of 150×10^6 m^3 (Amann, 2006; Bonnard et al., 2004). The instability spans an elevation range from 1700 to 2500 m, with the central zone currently moving southward at displacement rates of 10–20 cm/year. As displayed in Figure 1a, the instability features a relatively flat shoulder between 2200 and 2400 m, which transitions into a steeper 25–30° slope descending toward the valley floor at approximately 1550 m. The instability is laterally confined by the Strem River valley to the west and the Drun Tobel ravine to the south-east (Figure 1a). Due to the dominance of toppling as the primary deformation mechanism combined with the absence of an established sliding surface, we refer to this feature as a 'slope instability' rather than a 'landslide' (Amann, 2006; Hungr et al., 2014).

3.1 Geological & Geomorphological setting

The CdV instability is situated at the southern boundary of the Aar Massif, a region predominantly composed of granite and granodioritic gneiss (Abrecht, 1994; Kasperski et al., 2010). Locally, the CdV geology is characterized by competent gneisses in the upper section and weaker lithologies, such as incompetent gneisses, schists, and kakiritic rocks, in the lower slope area (Amann, 2006). Notably, the kakiritic rock forms a prominent outcrop at the southeastern landslide margin, comprising the so-called Drun Tobel. The CdV site features steeply dipping Alpine foliation and a complex fracture network, with three principal joint sets identified (Amann, 2006). Shear zones with reduced shear strength relative to the surrounding gneissic rock play a critical role in slope destabilization. The rock mass is highly fractured and disintegrated, as evidenced by the lack of surface water runoff on the western slope (Amann, 2006).

Geomorphological features such as graben structures, tension cracks, and sagging, as highlighted in Figure 2, indicate an overall extensional regime, particularly along the northern and eastern boundaries of the instability (Amann, 2006). In the central region, a high density of E–W striking anti-scarp structures suggests predominant toppling deformation oriented toward the south–south-west (Figure 2). The western and southeastern margins of the slope, corresponding to the Val Strem and Drun Tobel, respectively, are actively shaped by gullying and rockfall processes.

Structural and hydrological analyses by Amann (2006) suggest a transition zone between disintegrated and intact rock at depths of approximately 100–200 m in the central area. This depth estimate is consistent with Kleinbrod et al. (2017), who conducted the only seismic study at CdV to date analyzing ambient vibration polarization and spectral properties. The results by Kleinbrod et al. (2017) also suggested several isolated, less-fractured, block-like structures at depths of 35–150 m in the northeastern sector. However, their measurements were sparsely distributed and confined to the northeastern part of the slope, resulting in limited spatial resolution and only 1D subsurface information.

3.2 Long-term Displacement Monitoring

The earliest investigations of the CdV instability date back to 1942, followed by decades of regular deformation and displacement monitoring. During the past three decades, surface displacement observations have been significantly improved through the use of ground-based Global Navigation Satellite System (GNSS) campaigns (Amann, 2006) and digital image correlation of aerial photographs (Bickel et al., 2018). Between 1999 and 2002, Amann (2006) conducted a detailed analysis of surface displacements, as displayed in Figure 2. Mea-
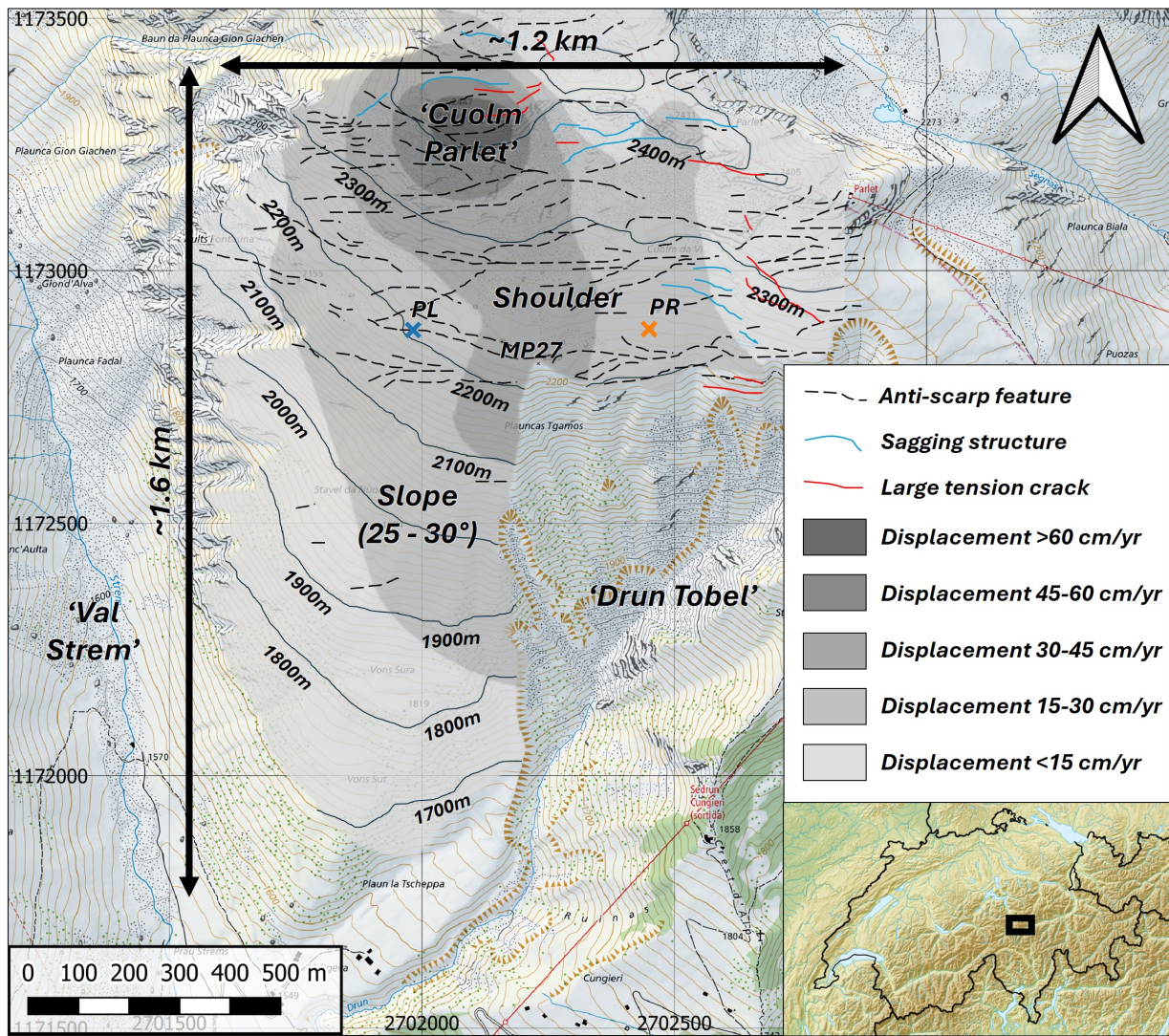
Figure 2 Topographic map of the Cuolm da Vi instability, overlaid with annual displacement rates from 1999 to 2002 and mapped geomorphological features (modified from Amann (2006)). MP27 marks the measuring point at the CdV instability centre, as suggested by Amann (2006). The blue and orange crosses denote the PL and PR tachymetry stations, respectively, of which the displacement time series are shown in Figure 3.

surements in the fast-moving Cuolm Parlet region indicated strong influences from local settlement dynamics unrelated to the deep-seated CdV instability. Excluding these local effects, the area near MP27 was identified as the fastest-moving part and the kinematic centre of the CdV instability, with annual displacements ranging from 20 to 40 cm during the study period (1999–2002) (Figure 2).

Since the 1999-2002 GNSS study, displacement at CdV has been continuously monitored as part of an early warning system using a laser-based tachymeter, installed in the village of Sedrun, measuring the distance to eight reflector poles at millimetre-level precision. Measurements are conducted every four hours and subsequently averaged to obtain daily displacement values. Figure 3 presents the derived displacement velocities for two example reflector poles PL and PR (locations indicated in Figure 2). Annual displacement rates in the central area of CdV decreased markedly after 2002, from 20–40 cm/year in 2002 to 10–20 cm/year in subsequent years. This reduction followed the exceptionally dry year of 2003, which presumably induced long-lasting,

large-scale changes in subsurface hydrological conditions (Amann, 2006). Despite being separated by approximately 500 metres, both reflectors display highly similar displacement patterns and magnitudes. The zoomed window in Figure 3b reveals pronounced and regular seasonal variations, with a distinct acceleration phase typically occurring from mid-to-late spring through early-to-mid summer. The magnitude and timing of this acceleration phase are likely correlated with the snowmelt period and therefore strongly depend on meteorological conditions from winter through summer. This phase is generally followed by a deceleration in late summer, that subsequently transitions into a longer period of oscillations around a background velocity of approximately 5 mm/month during winter time.

4 Research Objectives and Strategies

Our research at Cuolm da Vi (CdV) is centred around three overarching themes: 1) resolving the 3D structure and identifying key subsurface features, 2) study-
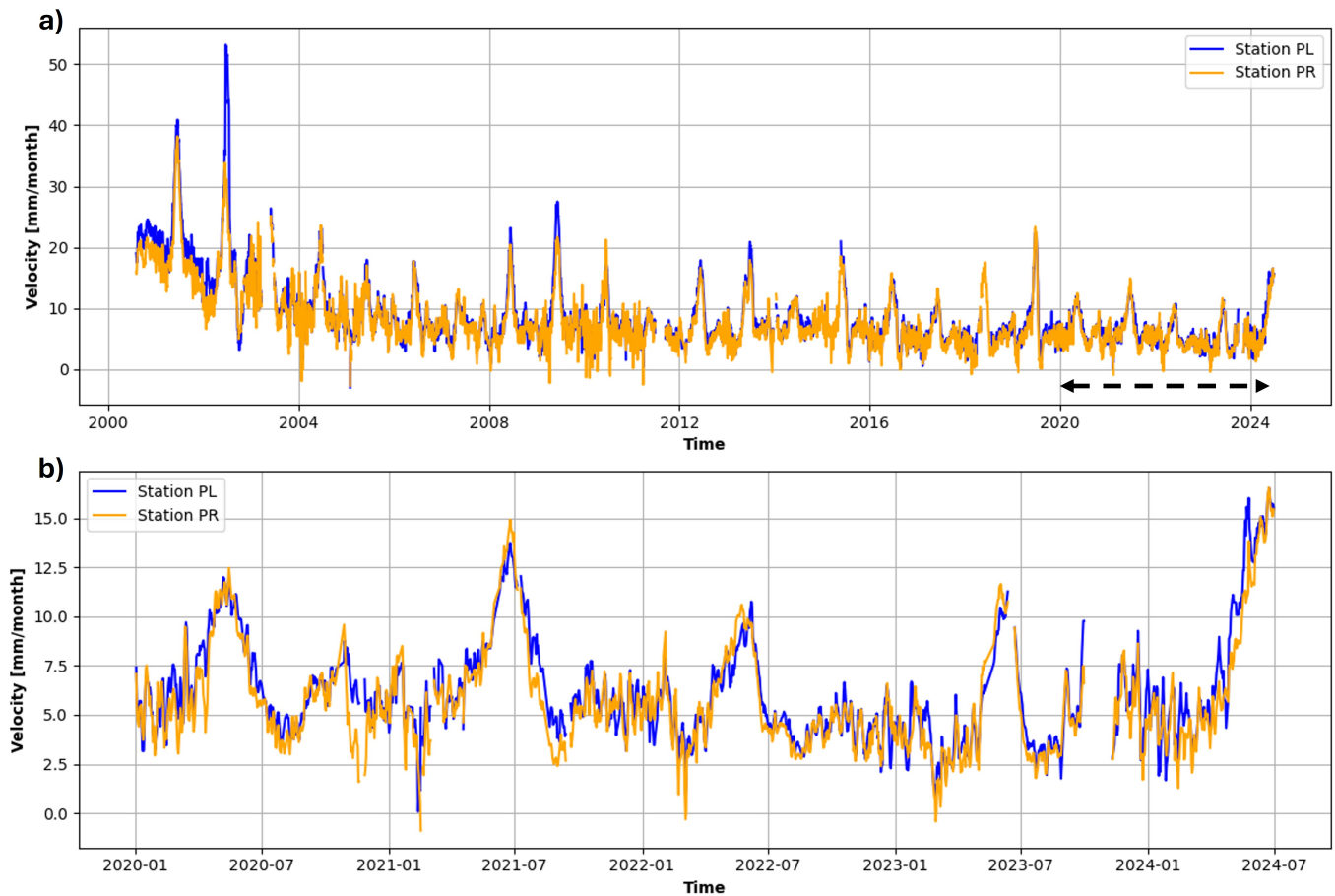
Figure 3 (a) Displacement velocity (mm/month) of reflector poles PL and PR derived from a time series extending back to the year 2000 (data provided by *Bonanomi-Gübeli AG*). Both reflector poles are located on the CdV shoulder, as indicated in Figure 2. To reduce significant daily measurement variation, the velocity data were smoothed using a 30-day running mean. (b) Zoomed window of the displacement velocity time series between January 2020 and July 2024 (dashed arrow in a)).

ing the slope dynamics and time-dependent processes, and 3) advancing nodal array and fibre-optic seismology for landslide characterization and monitoring. Because the targeted structures and processes likely span a wide range of spatial and temporal scales - from metres to kilometres and milliseconds to decades - multidisciplinary and very broadband observations are pivotal.

4.1   What Is the 3D Structure of Cuolm da Vi?

Determining the 3D subsurface structure of the CdV instability is essential for 1) accurately estimating the total unstable volume, 2) identifying structurally weak zones, and 3) mapping and characterizing tectonic features critical for geotechnical modelling and hazard assessment. Initial geotechnical, hydrological and seismic investigations by Amann (2006) and Kleinbrod et al. (2017) indicate a transition from disintegrated to integrated rock at about 100–200 m in the central area, but provide limited information about the full 3D structure.

We hypothesize that unstable and stable rock volumes can be distinguished on the basis of seismic velocity contrasts and that tectonic activity at key structural features results in the release of distinct seismic signals. Therefore, we identified 3D seismic imaging, in particular P-wave first-arrival traveltime tomography and full waveform inversion (e.g., Heincke et al., 2006b; Virieux

and Operto, 2009), ambient seismic vibration (ambient noise) interferometry for S-wave velocity imaging (e.g., Bensen et al., 2007; Rodríguez Tribaldos and Ajo-Franklin, 2021), and mapping of natural seismic source locations (e.g., Spillmann et al., 2007; Helmstetter and Garambois, 2010) as the main approaches to resolve the CdV internal structure.

Seismic data to address these hypotheses need to be acquired both on the stable and unstable parts of the slope, with 1) sufficiently dense spatial sampling to track seismic phases and record potentially weak natural signals, and 2) wide areal coverage to provide a broad range of source-receiver offsets and azimuth distribution for 3D imaging and source localization. Furthermore, the seismic data acquisition duration needs to be sufficiently long (up to several weeks) for ambient vibration imaging and spatially tracking the locations of natural slope seismicity.

4.2 How Do the Internal Dynamics, Material Properties and Seismic Signals Evolve Over Time?

Understanding the long-term dynamics of the CdV instability is essential for assessing slope stability and informing future modelling efforts. Of particular interest is the pronounced seasonality of the slope displacement, with consistent acceleration during the snowmelt period, highlighting time-dependent changes in internal stress and deformation mechanisms (Amann, 2006). However, the nature of these subsurface processes and their variability across different timescales remains poorly understood.

We hypothesize that internal stress redistribution and progressive damage lead to recurring seismic observables, such as microseismic events or changes in seismic wave velocities, that reflect cyclic mechanical behaviour. In particular, temporal variations in shear-wave velocity may indicate hydrologically induced changes in material properties (e.g., Mainsant et al., 2012; Larose et al., 2015), while the occurrence and temporal dynamics of seismic events may reveal evolving failure processes (e.g., Helmstetter and Garambois, 2010; Provost et al., 2018). By jointly analysing internal velocity changes and landslide-induced seismicity, we aim to capture both gradual and abrupt internal transitions and link them to environmental drivers such as snowmelt and precipitation phases.

Addressing these questions requires long-term seismic monitoring with dense sampling in space and time, particularly during the seasonal acceleration in spring, together with broadband sensitivity to be able to record a wide variety of seismic signals and ensure surface wave sensitivity across a wide range of depths and resolutions. The need for long-term dense spatial and temporal sampling makes fibre-optic technologies like Distributed Acoustic Sensing (DAS) particularly well-suited. The configuration must span a broad area of the instability with multiple cable orientations, ensuring adequate areal and azimuthal coverage.

4.3 How Can Distributed Fibre-Optic Sensing Be Effectively Leveraged for Slope Instability Monitoring?

Distributed fibre-optic sensing (DFOS) enables dense spatial and temporal sampling, making it well suited for both long-term seismic and deformation monitoring (DAS and DSS, respectively). However, this benefit comes with challenges: the sensing geometry is fixed by the cable layout, DAS and DSS are directionally sensitive, and installation in steep, alpine terrain can be logistically demanding.

Key questions arise around how to leverage the dense but constrained sampling of DFOS for effective instability monitoring. How can cable layout be optimized to capture relevant signals across the slope? What are the limits imposed by coupling conditions, terrain, and environmental influences like temperature? Additionally, using a single cable for multiple measurements (DAS and DSS) requires careful consideration of acquisition parameters and hardware compatibility.

To answer these questions, we require a combination of a strategically designed cable layout at the CdV shoulder with for example co-located nodal sensors. Controlled-source experiments and continuous data acquisition can help to evaluate the sensitivity, localization performance, and multi-purpose use of the fibre-optic configuration. This integrated approach can inform best practices for deploying DFOS in complex, real-world slope instability settings.

5 Sensor Network, Acquisition and Data Quality

To meet our research goals, we deployed a large-scale sensor network at the Cuolm da Vi (CdV) instability in summer 2022. This setup covered the accessible areas of both the stable and unstable regions of the CdV instability, as inferred from existing geological and geodetic analyses (Amann, 2006). The configuration included more than 1000 autonomous seismic nodes, along with a 6.5 km fibre-optic cable for Distributed Acoustic and Strain Sensing measurements (DAS & DSS), supplemented by several complementary sensor installations. A detailed map of the final sensor layout is shown in Figure 4. By integrating nodal and fibre-optic systems, we leverage the complementary strengths of both sensor types and their deployment options. The nodal array provides over 1000 local ground acceleration measurements in vertical direction and offers high deployment and coverage flexibility. However, seismic nodes can only record for a limited time and need to be collected before the data retrieval. In contrast, fibre-optic seismic sensing systems (DAS) collect distributed strain rate data along a fibre-optic cable and enable highly dense (metre-scale), continuous, and long-term data collection from one cable end (*Section 2.2*).

The deployment and data acquisition were carried out in three main phases. Following the initial deployment phase in June 2022, we conducted two major recording stages. The first recording phase in summer 2022 involved several weeks of continuous nodal and fibre-optic (DAS & DSS) recording and targeted on sensor validation and subsurface imaging. This included a large-scale controlled-source campaign (Figure 4), calibration of DAS acquisition parameters, and data comparison between co-located seismic nodes and fibre-optic measurements. Based on initial DAS data inspection, we extended the fibre-optic layout with a flag-shaped section at the CdV shoulder (Figure 4) to complete the permanent sensor installations. This final configuration supported the second acquisition phase that focused on monitoring: five months of continuous DAS recording from February to July 2023, simultaneously with the typical seasonal acceleration observed at CdV (Figure 3), and monthly 24-hour DSS measurements to capture the strain evolution over a full year. The acquisition timeline is summarized in Figure 5.
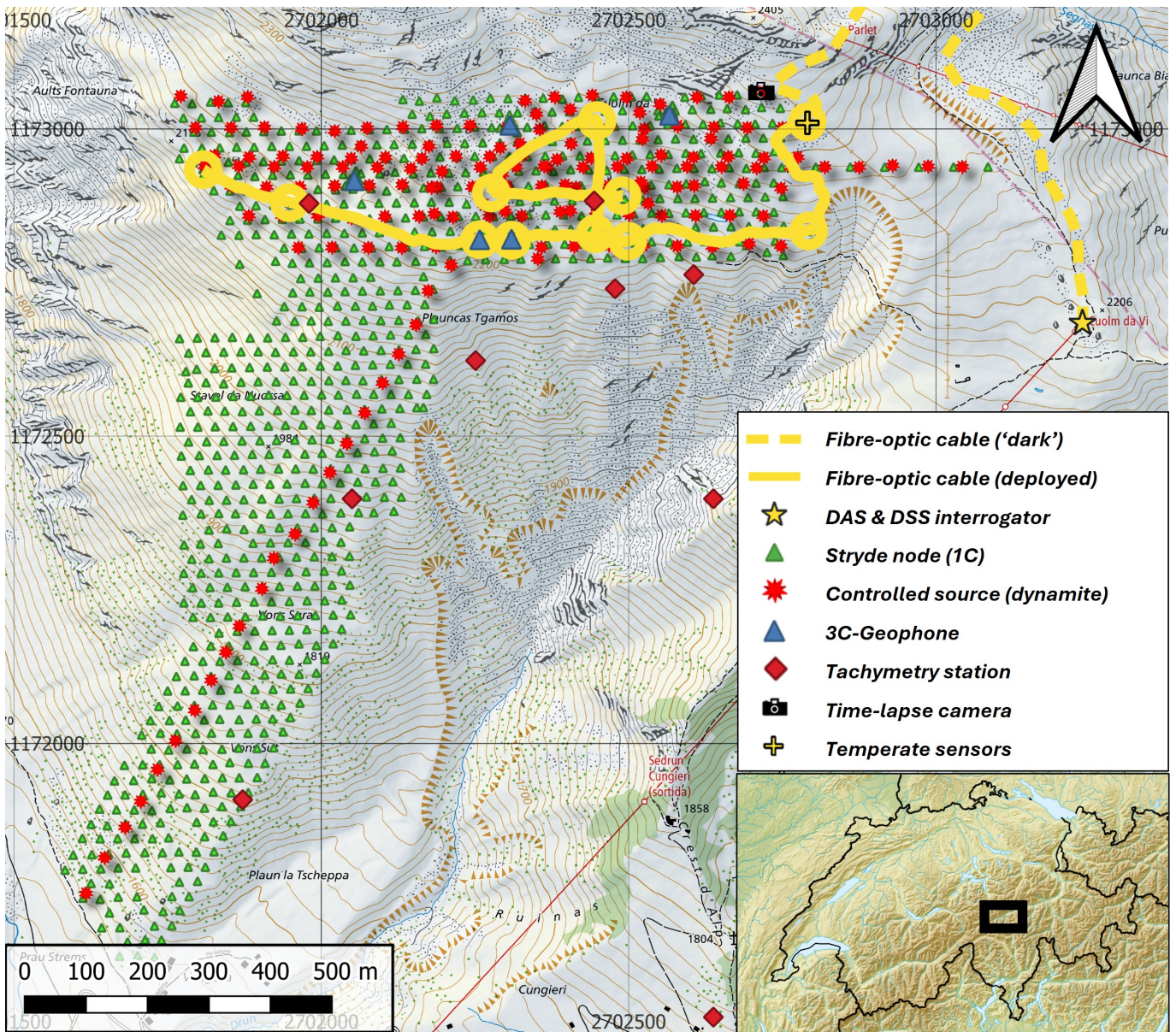
Figure 4 Overview of the sensor deployment at the CdV instability site. The map highlights 6.5 km of deployed fibre-optic cable including multiple 3-13 m loops (loop sizes exaggerated for clarity). The dashed yellow line indicates a pre-existing 'dark' cable installed for telecommunication purposes prior to this campaign. The main cable car station, which hosts the DAS and DSS interrogators, is marked with a yellow star. Green triangles denote the locations of deployed Stryde nodes, while red stars indicate dynamite shot points. Additional instrumentation includes five 3C-geophones, a time-lapse camera, temperature sensors co-located with the fibre-optic cable, and eight laser-based total stations.

5.1 Nodal Array of >1000 Seismic Sensors

5.1.1 Design

The CdV nodal configuration comprised 1048 one-component seismic nodes deployed across the accessible parts of the CdV slope and shoulder (Figure 4). A total of 878 nodes were arranged in an L-shaped hexagonal grid with a nominal sensor spacing of 28 m. We selected a hexagonal configuration for its uniform sensor-point spacing along three principal directions. These three orientations were well-aligned with the geometric shape of the CdV deployment area allowing for the formation of long, continuous receiver lines in W-E and SW-NE direction (Figure 4). The grid covered approximately 0.7 km², with maximum extents of 1.0 km (E-W) and 1.5 km (SW-NE).

To compare the seismic node data characteristics with DAS recordings, we installed 99 nodes along a 100 m fibre-optic cable section. We placed one vertical and one inline horizontal node every 2 m along the cable, exploiting the omni-directionality of the employed sensors. Fifteen nodes were used to create five 3C-sensor setups at the centres of selected fibre-optic loops, by collocating three sensors oriented in perpendicular directions mimicking a three-component measurement. Combined with fibre-optic loop recordings, this setup enables the local retrieval of 1D V_s subsurface models (Edme et al., 2024). Lastly, we arranged 40 nodes into four concentric small-scale arrays at the CdV shoulder ranging between 2 and 17 m in diameter, providing denser spatial sampling and designed for local array processing.
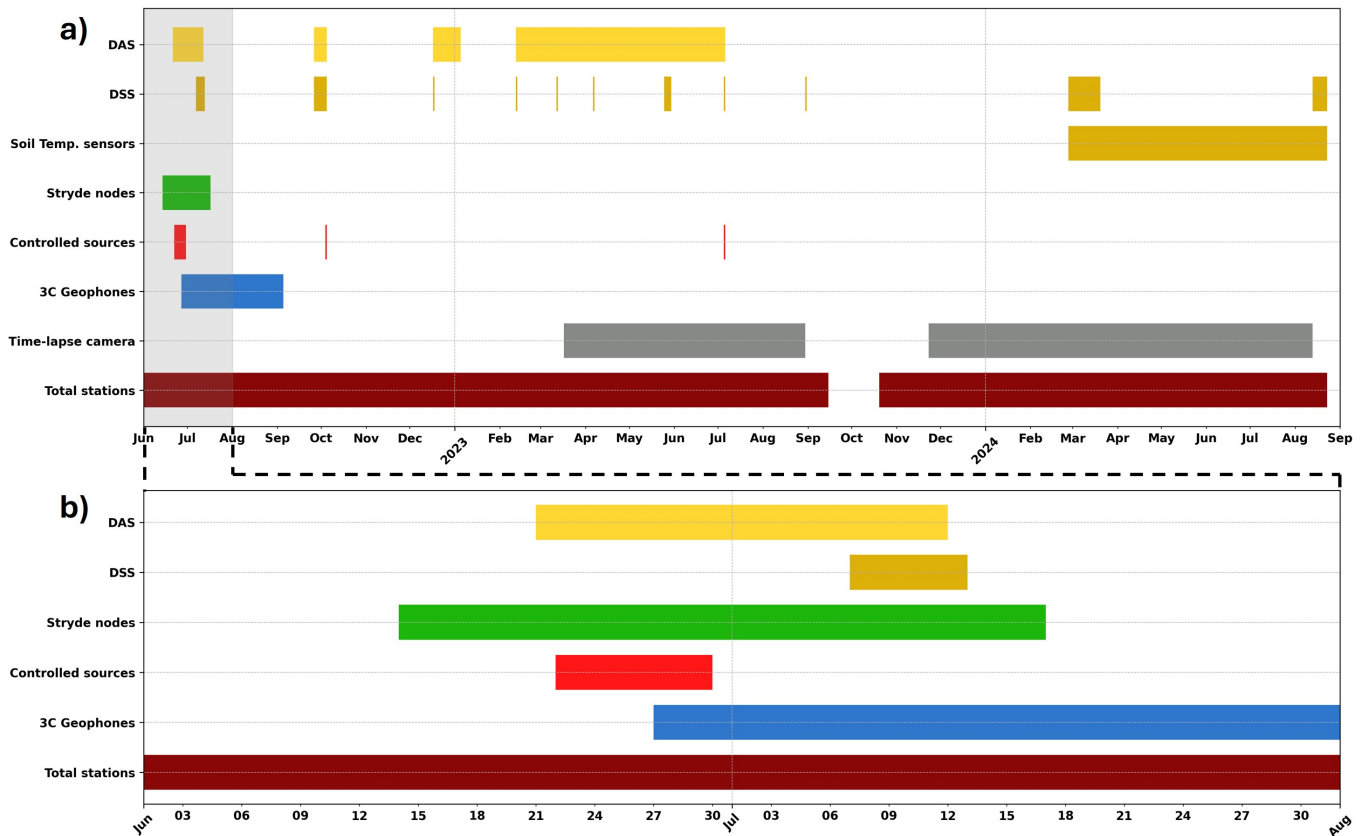
Figure 5 (a) Overview of the data acquisition timeline from 01 June 2022 to 01 September 2024. Each coloured bar represents the operational phase during which data for a given sensor were acquired. (b) Zoomed-in view of the summer 2022 period (01 June to 01 August).

5.1.2 Installation and Data Acquisition

We achieved the deployment of 1048 autonomous seismic STRYDE nodes (Manning et al., 2018; O'toole et al., 2024) with notable efficiency, facilitated by their compact size and lightweight design (150 grams) proving advantageous in the alpine terrain at CdV. Deployment and retrieval were completed within 4 to 5 days by three teams of two people each. Each node was installed by drilling a 10 cm deep hole followed by tightly installing the node.

We configured the nodes such that their internal batteries allowed for continuous recording of the ground acceleration at a sampling rate of 500 Hz for approximately 28 days, from mid-June to mid-July 2022 (Figure 5). We considered this duration adequate for conducting all planned controlled-source experiments and potential ambient vibration analyses. Data were stored internally within each node and retrieved after the campaign. To mitigate the effects of clock drift caused by factors such as temperature variations, each node was programmed to log GNSS timestamps every eight hours. This interval represented a balance between maximum timing inaccuracy (up to 1 ms in the extreme case) and saving battery power.

We found that GNSS reception for the majority of the nodes was limited due to the alpine terrain and surface conditions, particularly related to wet soil and dense grass cover. To improve GNSS signal quality, nodes were installed with approximately one-quarter

of their body above the surface, positioning the internal GNSS antenna above the ground. Nevertheless, a small amount of nodes (<5%) still experienced persistent GNSS-timing issues and were excluded from subsequent data processing. As a result of the partial installation above the surface, the node exposure and susceptibility to environmental noise significantly increased. Important noise factors include observed high-frequency wind noise and low-frequency, temperature-related sensor noise, which can be mitigated using adequate bandpass filtering.

The nodal array was initially designed in the Swiss LV95 coordinate system. For field installation, the deployment coordinates were converted to the WGS84 system, and nodes were positioned using GNSS receivers operating in the WGS84 frame. However, we found that the coordinate transformation introduced systematic shifts between planned and actual node locations, increasing from 0 m in the SW-corner to several metres in the NE part of the array (Figure 4). To ensure precise and consistent geometry information for data processing, the final node positions were surveyed with an accuracy of a few centimetres in the original LV95 coordinate system before node retrieval.

5.1.3 Wavefield Characteristics

Using a dense areal nodal layout at CdV provides the opportunity to appreciate the wavefield complexity, analyze the seismic wavefield characteristics, and infer sub-

surface properties in 3D. Figure 6 shows a 2D visualization of the wavefield propagation, generated by a controlled dynamite blast, in a projection onto the horizontal plane. This is displayed together with two source gathers along crossing W-E and SW-NE receiver lines (Figure 6b and c, receiver lines are marked as dashed lines in Figure 6a). Clear first arrivals, travelling at apparent velocities of around 600 m/s close to the source and at about 2000 m/s at a few hundred metres offset, are observable throughout the layout up to source-receiver offsets of 600–800 m, after bandpass filtering the data to 7.5–25 Hz. The first arrivals are followed by a cone of high-amplitude phases limited by apparent velocities ranging between around 400 and 600 m/s. We interpret these arrivals as aliased, and likely scattered surface waves. The complex nature of these arrivals is further illustrated in the wavefield snapshots in Figure 6a indicating significant wavefield scattering at topographic variations and subsurface heterogeneities.

5.2 Fibre-Optic Cable Configuration

5.2.1 Cable Design

In the summer of 2022, we installed a fibre-optic network comprising over 6.5 km of trenched cable to enable primarily Distributed Acoustic Sensing (DAS) and Distributed Strain Sensing (DSS) measurements (Figures 4 and 7). Because the deployed cables contain both single- and multi-mode fibres, the layout is also suitable for, for example, Distributed Temperature Sensing (DTS). The cable layout was designed to maximize coverage of the most active zones of the CdV instability, while ensuring adequate cable-to-ground coupling. To achieve this, the cable trajectory was aligned with soil-rich segments of the CdV shoulder, resulting in a 1.6 km trench primarily oriented east–west along a crest marking the boundary between the CdV shoulder and slope. To enhance the azimuthal sensitivity of the network, we expanded the installation in September 2022 by adding a flag-shaped extension in the central shoulder area (Figures 4 and 7). Additionally, eleven cable loops were incorporated along the cable trajectory (Figure 7), to 1) provide slack and accommodate for the differential slope movement and 2) enable omni-directional fibre-optic measurements.

The first approximately 1500 m of the network consists of pre-existing infrastructure ('dark fibre') managed by the local ski resort, as illustrated in Figures 4 and 7. The cable beginning is located in the basement of a cable car station proving shelter, full power supply, and internet connection. This enables the operation of up to two interrogators year-round, allowing, for example, simultaneous DAS and DSS recordings. At 1550 m cable distance, our newly installed cable was connected to the existing network at a ski lift cabin. The first kilometre of the new installation (1500–2500 m) consists of tight-buffered cable (orange in Figure 7), which is particularly suitable for DSS in addition to DAS measurements. Beyond this point, the layout is comprised of loose-tubed cable, which firstly continues westward. At approximately 3200 m optical distance, the cable reaches the end of the east–west trench

and doubles back along the same trench to return to the cabin. This return loop provides co-located recordings enabling, for example, channel stacking to improve signal quality. Furthermore, it facilitates DSS temperature correction at co-located tight-buffered and loose-tubed cable positions (Kechavarzi et al., 2016). Finally, the flag-shaped extension required a third cable to be added along the initial trench segment, in order to reach the central CdV shoulder.

5.2.2 Cable Installation

We carried out the fibre-optic cable installation in two phases: the east–west segment was completed in early June 2022, followed by the flag-shaped extension in late September 2022. Each phase began with trenching, using a petrol-powered handheld tool to cut narrow trenches of approximately 20–30 cm deep. In soft soil, trenching progressed up to 50-100 m per hour, while rocks and boulders had to be removed or bypassed locally, slowing down the process significantly. With a team of two to three people, an average trenching rate of 200–300 m per day was achieved.

We subsequently deployed the fibre-optic cables according to the layout in Figure 7. Avoiding sharp cable bends or kinks due to rocks at the trench base was a significant challenge. Logistically handling several kilometres of cable across rugged alpine terrain also proved demanding. Nevertheless, the cable deployment progressed at a pace similar to trenching (200-300 m/day). Once in place, trenches were backfilled with soil to improve cable-to-ground coupling.

We spliced the individual segments to form a continuous fibre-optic network (Figure 7). To enable simultaneous DAS and DSS data acquisition, two fibres were connected at each splicing point, establishing two continuous 6.5 km-long fibres along the entire network. In boulder-dominated areas, shallow trenches with limited soil cover were unavoidable, likely leading to stretches with locally reduced cable coupling. However, this coupling variability is an inherent aspect of fibre-optic deployments in such alpine environments.

5.3 Distributed Acoustic Sensing

5.3.1 Acquisition

We acquired all Distributed Acoustic Sensing (DAS) data using a Silixa iDAS V2 interrogator with a fixed 10 m gauge length, installed at the main cable car station (Figures 4 and 7). The data acquisition periods are shown in Figure 5 and include two primary campaigns: a three-week period in summer 2022, simultaneous with other sensor recordings (Figure 5b), and a five-month continuous acquisition during the first half of 2023, coinciding with the CdV acceleration phase (Figure 3b).

To enable dense spatial wavefield sampling, we used a 1 m channel spacing throughout all acquisition periods, resulting in approximately 6500 active data channels along the fibre-optic layout (Figure 7). Temporal sampling rates were chosen to balance resolution and data volume. We selected a 500 Hz sampling rate for the summer and fall 2022 campaigns (matching the Stryde
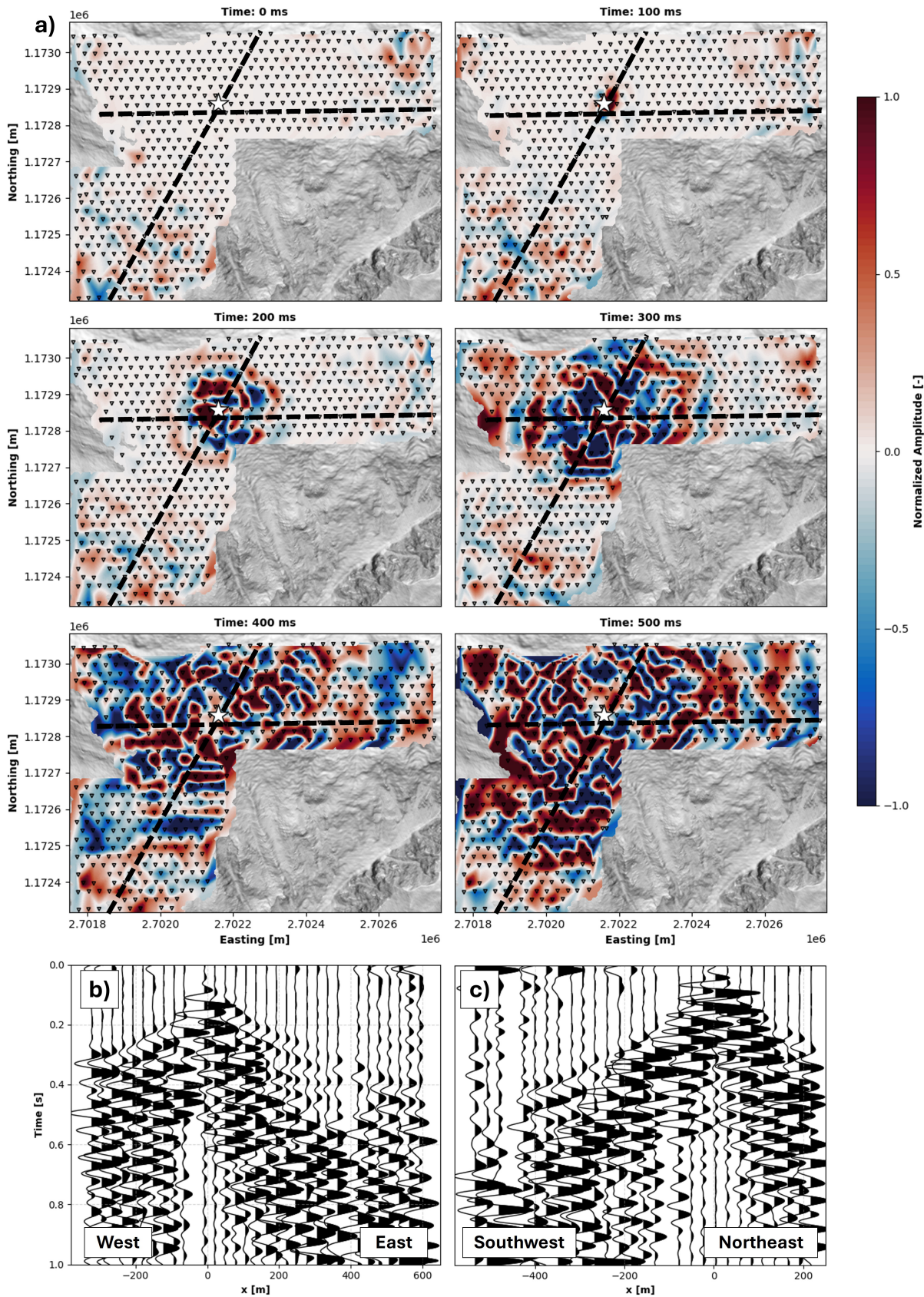
Figure 6 (a) 2D visualization of ground acceleration in the central area of the nodal array following a dynamite blast at $t = 0\,\text{s}$. Each panel shows a distinct time step, with elapsed time (in milliseconds) indicated above. Receiver locations are marked by small triangles, and the blast source is shown as a white star. Colour shading represents linearly interpolated, normalized ground acceleration amplitudes recorded by the nodal array and filtered between 7.5 and 25 Hz. The two black dashed lines denote an east-west and south-west–north-east receiver line of which source gathers are presented in (b) and (c), respectively, filtered using the same 7.5-25 Hz bandpass filter.
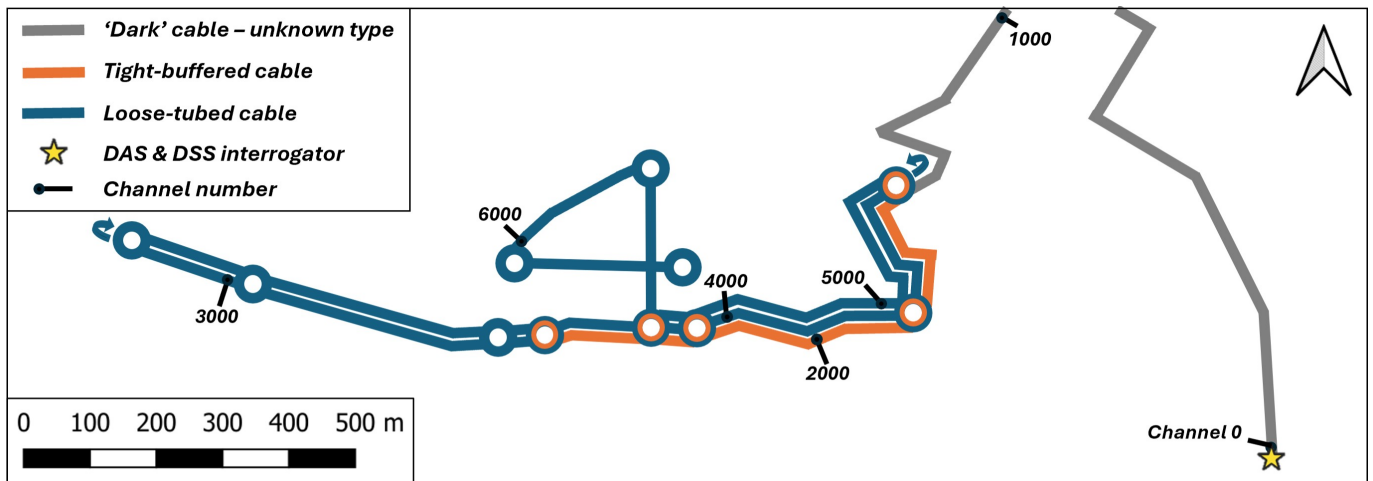
Figure 7 Schematic representation of the fibre-optic cable layout. Line colours indicate loose-tubed (blue) and tight-buffered cables (orange), and the location to install up to two interrogators is marked with a yellow star. Annotations label every 1000 metres along the cable, with 0 m corresponding to the point where the fibre exits the interrogator.

node temporal sampling), resulting in 400 GB of data collection per day. Considering our 0-200 Hz frequency range of primary interest, in combination with the logistical benefits of lower sampling rates for a 5-month acquisition period, a 250 Hz sampling rate was picked for the long-term 2023 campaign. Two 5 TB hard drives were used in parallel for daily data storage directly at the interrogator. These drives were regularly swapped on-site and the data were transferred to a large-capacity network storage system. To facilitate quick data exploration and practical data sharing, the raw dataset was downsampled to various resolutions.

We mapped each data channel to a specific spatial coordinate using a combination of location measurements and tap tests along the fibre-optic cable. A total of 239 GNSS-referenced tap tests were conducted across the entire configuration. These taps produced clear, identifiable signals in the raw DAS data, allowing direct mapping to specific channels. Intermediate channels were assigned coordinates through linear interpolation.

5.3.2 Seasonal Seismic Energy Levels

Between February and July 2023, we carried out a continuous five-month DAS acquisition at CdV (Figure 5). Figure 8 provides an overview of the seismic energy levels across various cable sections and frequency bands. The initial analysis reveals several notable patterns, most prominently the influence of the nearby ski area. This impact is particularly evident in the dark fibre and eastern cable sections, which intersect and run close to the ski infrastructure, respectively. In the 8–24 Hz frequency band (Figure 8), the operational cycles of ski lifts and subsequent slope grooming are clearly visible from the start of data acquisition (February 12, 2023) until the final operational day on April 10.

The dark fibre consistently exhibits lower noise levels than the sections deployed specifically for this study (Figure 7). Originally placed for telecommunication purposes, the dark fibre is installed in a conduit together with other cables, likely resulting in reduced ca-

ble coupling and smaller amplitudes. Nevertheless, its deeper burial depth (1-2 m) reduces susceptibility to atmospheric or other acoustic-ground coupled noise.

The self-deployed fibre sections (East, Flag, and West; Figure 7) consistently show higher noise levels during daytime compared to nighttime, independent of ski area operations. These elevated signals, presumably related to anthropogenic noise and associated with valley activities, increase notably after mid-May. This rise in noise amplitudes correlates with seasonal snowmelt, suggesting that the snow cover acts as an insulating layer, reducing the coupling of atmospheric and acoustic noise into the ground.

5.3.3 Comparison of DAS and Seismic Node Recordings

Seismic wavefield recordings of a controlled explosion measured at co-located DAS channels (1 m channel spacing) and node locations (2 m node spacing) are displayed in Figure 9. When comparing the two observations, one should keep in mind that DAS recordings correspond to horizontal strain rate measurements in cable direction, while vertical acceleration is measured with the seismic nodes. Hence, the two sensors exhibit different sensitivity to wavefield polarization. Furthermore, horizontal strain rate is proportional to local horizontal slowness and, hence, slow seismic phases such as surface waves may appear enhanced relative to first-arriving refracted body waves.

In the raw nodal recordings (Figure 9a), the air wave dominates the observed wavefield with very high amplitudes, which is largely absent in the DAS recordings. This discrepancy likely stems from installation differences: the DAS cable was buried by 20–30 cm, while the nodal sensors were partially exposed (25%) above the surface, increasing their susceptibility to air-coupled noise. Applying a 5–40 Hz bandpass filter effectively suppresses much of the high-frequency air wave in the nodal data (Figure 9b). The DAS recordings are less affected by this filtering, aside from a minor reduction
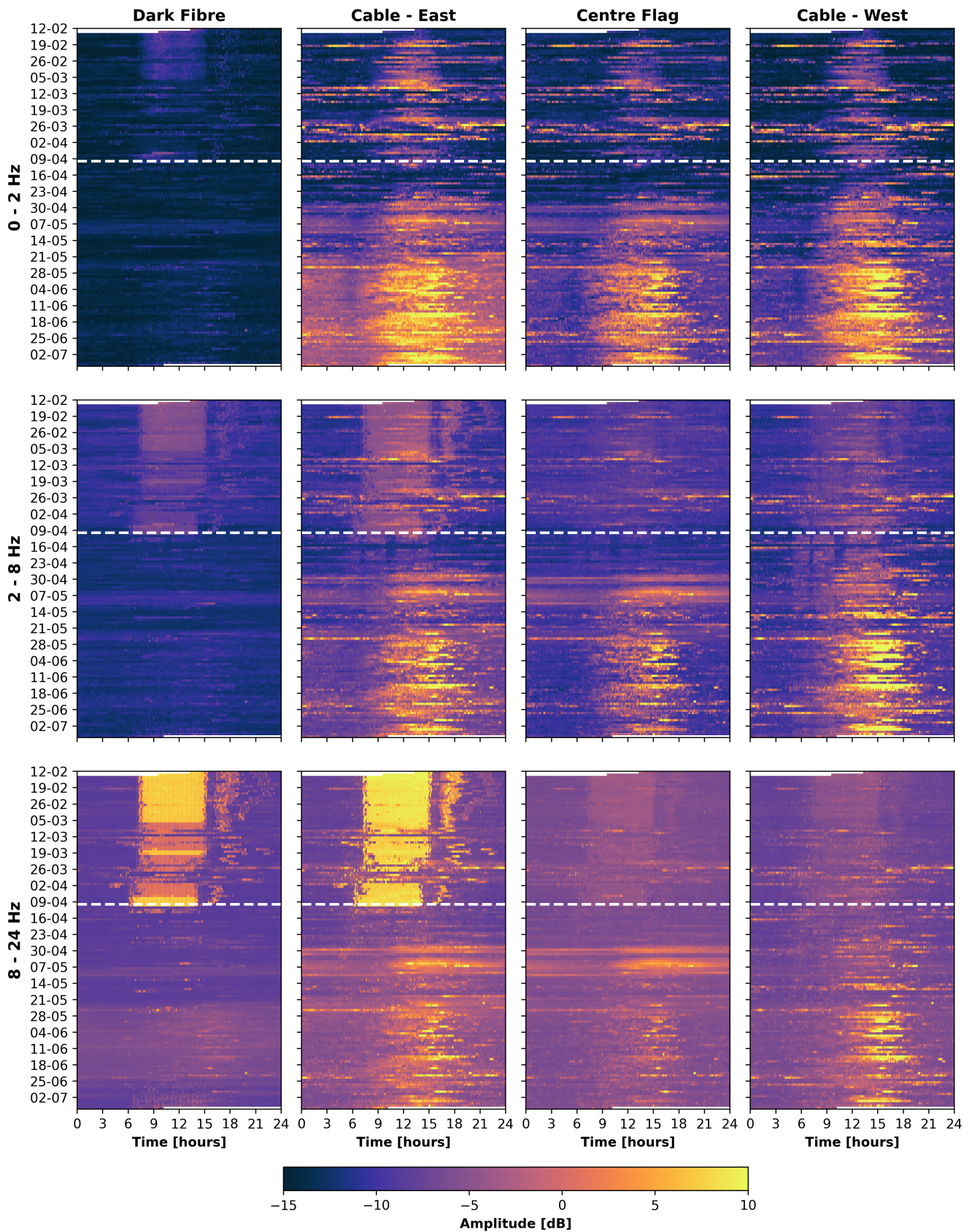
Figure 8   Seismic energy representation of the continuous 5-month DAS acquisition (February–July 2023) across four fibre-optic cable sections (columns) and three frequency bands (rows). Each subplot displays seismic energy in decibels (dB), with time of day (24-hour format) on the x-axis and calendar date (dd-mm) on the y-axis. Darker colours represent lower amplitudes; brighter yellow indicates higher amplitudes. The white dashed line marks the final operational day of the nearby ski area. Panels were generated by computing daily spectrograms using 60-second windows, averaged across all channels within each cable section, and subsequently averaged over the corresponding frequency band.

in high-frequency (optical) noise preceding the first arrival.

Despite the differing physical observables, the early wavefield characteristics appear consistent across both the DAS and node datasets. First-arriving energy is observed at comparable traveltimes, and multiple subsequent phases are captured similarly by both systems. The late wavefield, likely consisting of surface waves travelling at an apparent velocity of around 400 m/s, is more coherent in the DAS data possibly due to 1) the different sensitivity of the sensors to slow-travelling surface waves, and 2) the DAS gauge length of 10 m leading to smearing across channels. Nevertheless, the comparison shows that the 28 m node spacing of the regular grid is insufficient to capture unaliased surface wave phases.

5.4 Distributed Strain Sensing

5.4.1 Acquisition

We collected Distributed Strain Sensing (DSS) data using an Omnisens DITEST V4 interrogator installed at the main CdV cable car station (Figures 4 and 7). The acquisition timeline (Figure 5) highlights two key features of the dataset. First, extended continuous monitoring campaigns ranged from one week (e.g., July 2022, October 2022, May 2023, August 2024) to several weeks (February–March 2023). Second, monthly to bimonthly 24-hour acquisitions were performed from autumn 2022 to autumn 2023, covering one full year.

The DSS measurements were acquired using the BOTDR technique (Brillouin Optical Time Domain Reflectometry; Kurashima et al., 1993), with a spatial

sampling interval and resolution of 0.5 m and 1 m, respectively. A broad frequency scanning range of 10.4–11.2 GHz was used to capture both the Stokes and Anti-Stokes spectral peak across all cable sections. We selected an averaging count of 3000 individual readings to obtain stable measurements, leading to a measurement duration and interval of approximately 15 minutes. We acquired DSS data along the full cable layout, including the co-located tight-buffered segments (sensitive to both strain and temperature) and loose-tubed segments (primarily sensitive to temperature) (Figure 7).

5.4.2 Strain and Temperature Signatures

Raw data from the continuous DSS campaign in summer 2022 are shown in Figure 10. The variability of the Stokes spectral peak along the entire cable layout (Figure 10a) clearly differentiates the dark-fibre, tight-buffered, and loose-tubed segments by their distinct Brillouin backscattering frequencies. The pre-existing dark fibre section further appears to comprise multiple cable types.

In Figure 10b, we display the relative Brillouin frequency shifts in the tight-buffered cable section (sensitive to both temperature and strain) across five consecutive days, using the first measurement as a reference. We observe notable diurnal patterns across all channels, while in addition, a few localized anomalies stand out. One example is a pronounced ∼30 MHz shift, confined to a 5–10 m segment, around optical distance 2302 m (black arrow), which occurred on July 10.

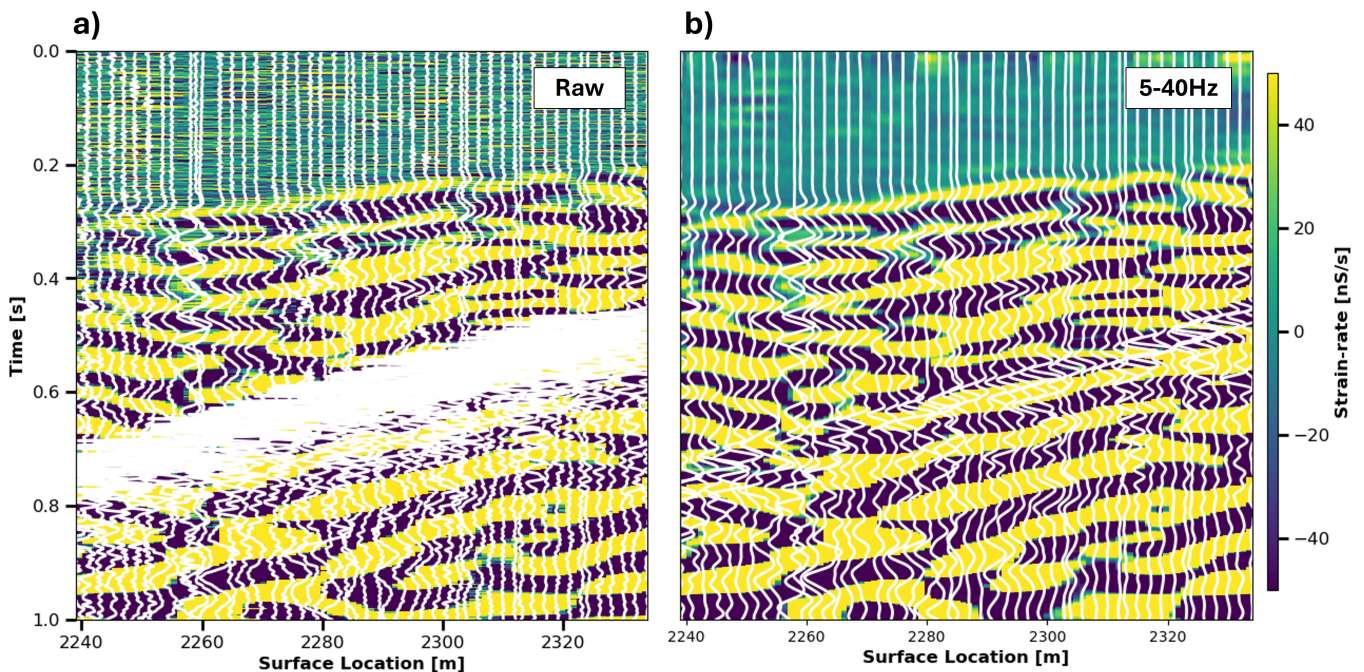The full five-day time series of this tight-buffered lo-

Figure 9 Comparison of fibre-optic and co-located vertical Stryde node recordings following a controlled source. The fibre-optic data are displayed as a yellow–blue background image, with the co-located Stryde node recordings overlaid as white traces. The source was predominantly inline, with a minimum offset of 150 m located on the right side of each panel. Fibre-optic data represent stacked signals from co-located channels of the forward and backward cables (Figure 7). (a) Unfiltered raw data. (b) Data after applying a 4th-order Butterworth bandpass filter between 5–40 Hz.
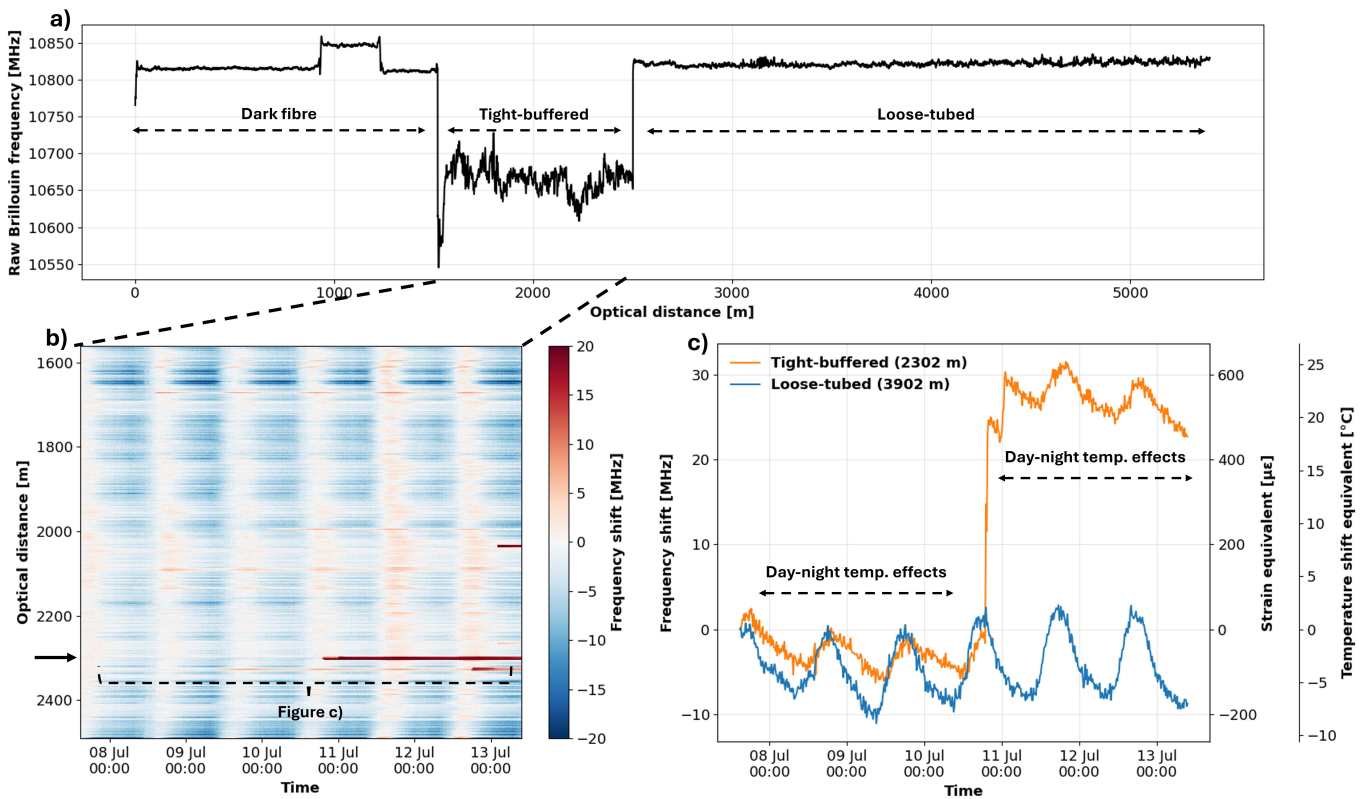
Figure 10 Distributed Strain Sensing (DSS) data from the continuous summer 2022 campaign. (a) Raw Stokes Brillouin frequencies along the full cable configuration for the first measurement on 8 July 2022, with annotated cable segments. Note that during this period, the fibre-optic flag extension was not installed yet, making the cable around 1000 m shorter compared to the full installation. (b) Relative Brillouin frequency shifts in the tight-buffered section over five consecutive days (8–13 July 2022), referenced to the first measurement. (c) Time series from the tight-buffered channel at 2302 m optical distance (orange, marked in (b)) and a co-located loose-tubed channel at 3902 m optical distance (blue). The strain and temperature shift equivalent axes are approximations based on silica-based Brillouin strain and temperature coefficients defined by Łakomski et al. (2025).

cation (2302 m optical distance) and co-located loose-tubed channel (3902 m optical distance) are presented in Figure 10c. Both exhibit clear diurnal temperature-induced signals, which are more pronounced in the loose-tubed cable (temperature equivalents of $\sim$8 °C compared to $\sim$5 °C in the tight-buffered cable). The observed differences in amplitude and phase of these tight-buffered and loose-tubed periodic signals are likely caused by slight differences in cable properties and burial depth of the two cables.

On the evening of July 10, the tight-buffered channel shows a sharp $\sim$25 MHz step, followed two hours later by a smaller $\sim$5 MHz shift. As these features are absent in the loose-tubed data, we interpret them as local rapid strain events equivalent to tensile strains of $\sim$500 and $\sim$100 $\mu\varepsilon$, respectively. To resolve smaller strain changes in the tight-buffered data, a correction for the temperature component is required. The clear presence of day-night temperature variations in both cable recordings (Figure 10c) demonstrates the potential for using the co-located cable types to separate the temperature and strain component in the tight-buffered data (Kechavarzi et al., 2016).

5.5 Controlled Seismic Source Experiment

After the installation of the nodal array and the initial fibre-optic configuration, we conducted a controlled-source seismic campaign between June 22 and June 29, 2022 (Figure 5). The main purpose of the controlled-source survey was to collect seismic data for subsurface imaging using, for example, first-arrival travel-time tomography and full waveform inversion. The controlled-source layout comprised two main components: a source-point grid and two additional source lines (Figure 4). The grid followed a hexagonal pattern with 95 source points spaced at a nominal 56 m, corresponding to twice the nodal array spacing of 28 m. This source spacing represented a trade-off between achieving sufficient ray coverage for a 3D first-arrival travel-time inversion and acquisition time. The source positions were designed to coincide with the centres of the equilateral triangles formed by the nodal array.

Due to the steep terrain at the CdV slope (Figure 1), extending the source grid in this area was not feasible. Instead, two additional shot lines were conducted both crossing the proposed stable-unstable transition zones (Figure 4). The west-east shot line ($\sim$1.4 km) traversed the entire CdV shoulder, while the southwest–northeast line ($\sim$1.6 km) spanned the full slope.

The shot holes, ranging in depth from 0.4 m to 1.0 m, were drilled using a battery-powered drilling device and charged with 50–60 grams of Riodin explosive. This charge size provided sufficient energy for traveltime observations at offsets exceeding 500 m (Figure 6). A three-person team was able to conduct up to 20–30 shots per day. The significant variation in shot hole depths (0.4 m to 1.0 m) was primarily the consequence of highly variable subsurface conditions. Following the completion of the fibre-optic flag-shaped extension, an additional 20 explosions were conducted on the 4th of October, 2022, to be able to evaluate, for example, the seismic source localization performance of the deployed DAS configuration.

5.6 Complementary Sensors

Several additional sensors were installed in order to complement the analysis of the nodal array and fibre-optic data. From June 27 to September 5, 2022, we deployed five 3C-geophones at the CdV shoulder (Figures 4 and 5) sampling at 400 Hz using Digos digitizer units. In contrast to the Stryde nodes, these sensors were fully buried and recorded 3-component data.

At the start of the 5-month DAS acquisition campaign, a time-lapse camera was installed at a lookout point in the northeastern section of the study area (Figures 4 and 5). Positioned with a clear view of the CdV shoulder, the camera provided continuous visual monitoring (12-min interval) of snow cover and potential seismic noise sources, including weather events, animal activity, and human presence. These visual records support the classification and interpretation of anthropogenic and environmental noise signatures present in the fibre-optic data.

In parallel with the ongoing DSS acquisitions throughout 2024, several soil temperature sensors were installed at depths comparable to the fibre-optic cables (approximately 20–30 cm below the surface). These sensors provide independent measurements of near-surface temperature variations, supporting a more accurate characterization of the thermal component in the DSS data and improving the reliability of temperature correction analyses.

6 Discussion

6.1 Installation of an Alpine Multi-Sensor Seismic Network: Lessons Learned

The different stages of full data set acquisition, including pre-campaign planning and post-campaign data management, are time-intensive. An approximate overview of the associated time requirements for our case study is provided in Table 1. We emphasize that these estimates are strongly dependent on local site conditions and the specific objectives of the data acquisition. For example, if the measurements are conducted in more accessible and less challenging alpine terrain, both personnel involvement and overall time requirements may be substantially reduced.

To successfully complete the installation of a seismic network including several kilometres of fibre-optic cable and over 1000 nodes, it was pivotal to take the challenging Alpine environment into account. Fibre-optic cable trenches could only be installed at soil-rich crests, where 20–30 cm slits could be installed with a handheld trenching device to ensure adequate cable coupling and protection in the harsh environment. However, the limited presence of continuous soil-rich stretches also restricted our flexibility for placing the cable. Therefore, the shape of the fibre-optic layout may not be ideal for all data applications.

Deploying more than 1000 sensors across terrain with approximately 800 m of elevation change was possible only because of their low weight (150 g) and small dimensions, which allowed one person to carry up to 100 nodes in a dedicated backpack. This logistical advantage outweighed the fact that the nodes only provided 1-component (1C) ground acceleration measurements, as opposed to 3C-receivers that enable analyses relying on wavefield polarization. Although the omnidirectional node design in principle allows three 1C-nodes to be combined into a 3C-unit, for this deployment we prioritized dense spatial sampling and associated spatial resolution over 3C-measurements.

We underestimated the shadowing of the topography and the impact of the Alpine soil and vegetation on the GNSS reception of the deployed nodes. We were forced to install the sensors less deep (about a quarter of the sensor above the surface) than originally planned. This ensured that the internal GNSS receivers were sufficiently above the ground, but also resulted in elevated wind noise susceptibility and reduced coupling.

At CdV, ambient noise energy levels are characterized by a marked change around April–May. After late April, diurnal variations become much more pro-

Activity	Personnel	Duration
Prior to field campaign		
Experiment design and planning	1–2	4 months (50% effort)
Field campaign		
Nodal array deployment	6	5 days
Nodal array retrieval	4	5 days
Fibre-optic cable deployment	4	15 days
Fibre-optic measurement campaigns	2	20 days
Controlled-source experiment	3	8 days
Complementary measurements	1	15 days
Following field campaign		
Data set management and archiving	1	2 months

Table 1 Approximate overview of personnel involvement and time requirements for the different stages of data set acquisition.

nounced compared to winter, with maximum energy levels being about 5–10 dB higher in summer than in winter. We attribute this difference to the damping effect of the winter snow cover, which typically melts around April–May. Elevated summer noise levels may complicate the detection of weak seismic events, although appropriate processing such as bandpass filtering can mitigate the noise impact.

Ski-lift operations are clearly visible in fibre-optic recordings close to the ski area, where they dominate the high-frequency band above 8 Hz. In contrast, the low-frequency spectrum (<8 Hz) remains relatively unaffected across the entire layout. Besides that, cable sections located more than ∼500 m from the ski lifts (central and western parts) show little to no impact in either band.

The multi-sensor configuration and data acquisition at CdV is an ongoing project including potential future extensions. A particularly valuable network addition would be the deployment of a fibre-optic cable extending from the CdV shoulder downslope into the valley, complementing the nodal array in this area. This would enable long-term monitoring of seismicity and strain patterns along the slope. To date, this extension has not been realised due to steep topography and associated logistical challenges; however, it appears feasible with additional resources and could provide substantial added value. If fibre-optic deployment along the slope remains impractical, alternative strategies for long-term seismic monitoring could be pursued, for example through the installation of several long-term seismic stations.

6.2 Implications for Seismic Measurements

The successful recording of body and surface waves from explosions fired during summer daytime (Figure 6), when highest seismic ambient noise levels were observed in both the nodal and DAS measurements, yielded valuable data for subsurface imaging (e.g., traveltime tomography, Kiers et al., 2026). Furthermore, considering that small explosive charges of around 50 g release limited energy, we are confident that the DAS layout likely allows recording data with a sufficiently high signal-to-noise ratio to detect and interpret natural seismic signals even during the noisier periods.

The recorded seismic wavefield is dominated by slow-propagating surface waves with apparent velocities of 400–600 m/s. Given the highest observed signal frequencies of approximately 40 Hz, the shortest apparent wavelengths are about 10 m. As a result, the 28 m node spacing results in the surface wave recordings being aliased at frequencies above 6–7 Hz. Based on these wavefield characteristics, we recommend, for optimized long-term DAS recording at CdV, a DAS channel spacing of 5 m (or less) to adequately sample the dominant surface waves.

7 Conclusions

We present the installation and data examples of a comprehensive seismic and fibre-optic monitoring network at the Cuolm da Vi (CdV) slope instability, one of the largest active deep-seated instabilities in the Alps. The deployment of over 1000 nodal seismic sensors and 6.5 km of fibre-optic cable for Distributed Acoustic and Strain Sensing provides a unique monitoring setup covering a wide range of spatial and temporal scales: from metres to kilometres and milliseconds to years. This enables high-resolution characterization and monitoring of different subsurface structures and time-dependent deformation processes across different dimensions.

The integration of nodal and fibre-optic technologies provides complementary strengths in the context of instability monitoring: broad spatial coverage and flexibility from nodal arrays, combined with dense, continuous and long-term fibre-optic sensing. A first data screening demonstrates the capacity to answer open research questions using a wide range of seismic analysis techniques for controlled-source and continuous seismic recordings, as well as long-term strain sensing. This dataset opens the door to detailed investigations into the CdV structure, internal damage evolution, and the interplay between environmental drivers and mechanical response. Furthermore, this integrated seismic sensor network represents a significant step toward multi-sensor monitoring strategies for slope instability hazard analysis and risk assessment.

GNSS instrumentation. Finally, we would like to sincerely thank the editor and the reviewers for the thorough and constructive evaluation, including the helpful comments and suggestions allowing us to improve the quality and clarity of the manuscript.

Data and code availability

Funding Sources

Competing interests

The authors acknowledge that there are no conflicts of interest recorded.

References

Abrecht, J. Geologic Units of the Aar Massif and Their Pre-Alpine Rock Associations: A Critical Review. *Schweizerische Mineralogische und Petrographische Mitteilungen*, 74:5–27, Jan. 1994.

Acharya, A. and Kogure, T. Application of novel distributed fibre-optic sensing for slope deformation monitoring: a comprehensive review. *International Journal of Environmental Science and Technology*, Dec. 2022. doi: 10.1007/s13762-022-04697-5.

Acharya, A. and Kogure, T. Advances in fibre-optic-based slope reinforcement monitoring: A review. *Journal of Rock Mechanics and Geotechnical Engineering*, June 2024. doi: 10.1016/j.jrmge.2024.03.022.

Ajo-Franklin, J. B., Dou, S., Lindsey, N. J., Monga, I., Tracy, C., Robertson, M., Rodriguez Tribaldos, V., Ulrich, C., Freifeld, B., Daley, T., and Li, X. Distributed Acoustic Sensing Using Dark Fiber for Near-Surface Characterization and Broadband Seismic Event Detection. *Scientific Reports*, 9(1):1328, Dec. 2019. doi: 10.1038/s41598-018-36675-8.

Alimohammadlou, Y., Najafi, A., and Yalcin, A. Landslide process and impacts: A proposed classification method. *CATENA*, 104: 219–232, May 2013. doi: 10.1016/j.catena.2012.11.013.

Amann, F. *Großhangbewegung Cuolm Da Vi (Graubünden, Schweiz) Geologisch-geotechnische Befunde und numerische Untersuchungen zur Klärung des Phänomens*. PhD thesis, Universität Erlangen-Nürnberg, 2006.

Bensen, G. D., Ritzwoller, M. H., Barmin, M. P., Levshin, A. L., Lin, F., Moschetti, M. P., Shapiro, N. M., and Yang, Y. Processing seismic ambient noise data to obtain reliable broad-band surface wave dispersion measurements. *Geophysical Journal International*, 169(3):1239–1260, June 2007. doi: 10.1111/j.1365-246X.2007.03374.x.

Bertello, L., Berti, M., Castellaro, S., and Squarzoni, G. Dynamics of an Active Earthflow Inferred From Surface Wave Monitoring. *Journal of Geophysical Research: Earth Surface*, 123(8): 1811–1834, 2018. doi: 10.1029/2017JF004233.

Bickel, V., Manconi, A., and Amann, F. Quantitative Assessment of Digital Image Correlation Methods to Detect and Monitor Surface Displacements of Large Slope Instabilities. *Remote Sensing*, 10(6):865, June 2018. doi: 10.3390/rs10060865.

Bonnard, C., Dewarrat, X., and Noverraz, F. The Sedrun Landslide. In *Identification and Mitigation of Large Landslide Risks in Europe*, Advances in Risk Assessment. IMIRILAND Project, pages 227–252. Taylor and Francis, Balkema, Leiden, 2004.

Bontemps, N., Lacroix, P., Larose, E., Jara, J., and Taipe, E. Rain and small earthquakes maintain a slow-moving landslide in a persistent critical state. *Nature Communications*, 11(1):780, Feb. 2020. doi: 10.1038/s41467-020-14445-3.

Brenguier, F., Shapiro, N. M., Campillo, M., Ferrazzini, V., Duputel, Z., Coutant, O., and Nercessian, A. Towards forecasting volcanic eruptions using seismic noise. *Nature Geoscience*, 1(2):126–130, Feb. 2008. doi: 10.1038/ngeo104.

Clague, J. J., Roberts, N. J., and Stead, D. Landslide hazard and risk. *Landslides: Types, Mechanisms and Modeling – Cambridge, University Press, United Kingdom*, pages 1–9, 2012.

Corominas, J., Moya, J., Lloret, A., Gili, J. A., Angeli, M. G., Pasuto, A., and Silvano, S. Measurement of landslide displacements using a wire extensometer. *Engineering Geology*, 55(3):149–166, Feb. 2000. doi: 10.1016/S0013-7952(99)00086-1.

Edme, P., Kiers, T., Paitz, P., and Robertsson, J. Divergence-Based Local Near-Surface Characterization with Distributed-Acoustic-Sensing. In *85th EAGE Annual Conference & Exhibition*, volume 2024, pages 1–5. European Association of Geoscientists & Engineers, 2024. doi: 10.3997/2214-4609.2024101569.

Erismann, T. H. and Abele, G. *Dynamics of Rockslides and Rockfalls*. Springer Science & Business Media, Apr. 2001.

Finnegan, N. J., Brodsky, E. E., Savage, H. M., Nereson, A. L., and Murphy, C. R. Seasonal Slow Landslide Displacement Is Accommodated by Mm-Scale Stick-Slip Events. *Geophysical Research Letters*, 49(20):e2022GL099548, 2022. doi: 10.1029/2022GL099548.

Froude, M. J. and Petley, D. N. Global fatal landslide occurrence from 2004 to 2016. *Natural Hazards and Earth System Sciences*, 18(8):2161–2181, Aug. 2018. doi: 10.5194/nhess-18-2161-2018.

Gili, J. A., Corominas, J., and Rius, J. Using Global Positioning System techniques in landslide monitoring. *Engineering Geology*, 55(3):167–192, Feb. 2000. doi: 10.1016/S0013-7952(99)00127-1.

Glueer, F., Mreyen, A.-S., Cauchie, L., Havenith, H.-B., Bergamo, P., Halló, M., and Fäh, D. Integrating Seismic Methods for Characterizing and Monitoring Landslides: A Case Study of the Heinzenberg Deep-Seated Gravitational Slope Deformation (Switzerland). *Geosciences*, 14(2):28, Jan. 2024. doi: 10.3390/geosciences14020028.

Goldswain, G. Advances in seismic monitoring technologies. In *Proceedings of the Second International Conference on Underground Mining Technology*, pages 173–188. Australian Centre for Geomechanics, Perth, 2020.

Handwerger, A., Fielding, E., Sangha, S., and Bekaert, D. Landslide Sensitivity and Response to Precipitation Changes in Wet and Dry Climates. *Geophysical Research Letters*, 49(2): e2022GL099499, July 2022. doi: 10.1029/2022GL099499.

Handwerger, A. L., Huang, M.-H., Fielding, E. J., Booth, A. M., and Bürgmann, R. A Shift from Drought to Extreme Rainfall Drives

a Stable Landslide to Catastrophic Failure. *Scientific Reports*, 9 (1):1569, Feb. 2019. doi: 10.1038/s41598-018-38300-0.

Hansen, S. M. and Schmandt, B. Automated detection and location of microseismicity at Mount St. Helens with a large-N geophone array. *Geophysical Research Letters*, 42(18):7390–7397, 2015. doi: 10.1002/2015GL064848.

Heincke, B., Green, A. G., van der Kruk, J., and Willenberg, H. Semblance-Based Topographic Migration (SBTM): A Method for Identifying Fracture Zones in 3D Georadar Data. *Near Surface Geophysics*, 4:79–88, 2006a. doi: 10.3997/1873-0604.2005034.

Heincke, B., Maurer, H., Green, A. G., Willenberg, H., Spillmann, T., and Burlini, L. Characterizing an unstable mountain slope using shallow 2D and 3D seismic tomography. *GEOPHYSICS*, 71(6): B241–B256, Nov. 2006b. doi: 10.1190/1.2338823.

Helmstetter, A. and Garambois, S. Seismic monitoring of Schilienne rockslide (French Alps): Analysis of seismic signals and their correlation with rainfalls. *Journal of Geophysical Research: Earth Surface*, 115(3), 2010. doi: 10.1029/2009JF001532.

Hopp, C., Guglielmi, Y., Rinaldi, A. P., Soom, F., Wenning, Q., Cook, P., Robertson, M., Kakurina, M., and Zappone, A. The Effect of Fault Architecture on Slip Behavior in Shale Revealed by Distributed Fiber Optic Strain Sensing. *Journal of Geophysical Research: Solid Earth*, 127(1):e2021JB022432, 2022. doi: 10.1029/2021JB022432.

Hudson, T. S., Kettlety, T., Kendall, J.-M., O'Toole, T., Jupe, A., Shail, R. K., and Grand, A. Seismic Node Arrays for Enhanced Understanding and Monitoring of Geothermal Systems. *The Seismic Record*, 4(3):161–171, July 2024. doi: 10.1785/0320240019.

Hungr, O., Leroueil, S., and Picarelli, L. The Varnes classification of landslide types, an update. *Landslides*, 11(2):167–194, Apr. 2014. doi: 10.1007/s10346-013-0436-y.

Iten, M., Ravet, F., Niklès, M., Facchini, M., Hertig, T., Hauswirth, D., and Puzrin, A. Soil-embedded fiber optic strain sensors for detection of differential soil displacements. In *Proc. of 4th International Conference on Structural Health Monitoring on Intelligent Infrastructure (SHMII-4)*, pages 22–24, 2009.

Jemec Auflič, M., Bezak, N., Šegina, E., Frantar, P., Gariano, S. L., Medved, A., and Peternel, T. Climate change increases the number of landslides at the juncture of the Alpine, Pannonian and Mediterranean regions. *Scientific Reports*, 13(1):23085, Dec. 2023. doi: 10.1038/s41598-023-50314-x.

Jongmans, D. and Garambois, S. Geophysical investigation of landslides : a review. *Bulletin de la Société Géologique de France*, 178(2):101–112, Mar. 2007. doi: 10.2113/gssgfbull.178.2.101.

Jongmans, D., Hemroulle, P., Demanet, D., Renardy, F., and Vanbrabant, Y. Application of 2D electrical and seismic tomography techniques for investigating landslides. *European Journal of Environmental and Engineering Geophysics*, 5:75–89, Jan. 2000. doi: 10.3997/2214-4609.201406464.

Kang, J., Walter, F., Paitz, P., Aichele, J., Edme, P., Meier, L., and Fichtner, A. Automatic monitoring of rock-slope failures using distributed acoustic sensing and semi-supervised learning. *Geophysical Research Letters*, 51(19):e2024GL110672, 2024. doi: 10.22541/essoar.171820821.18866285/v1.

Kannaujiya, S., Chattoraj, S. L., Jayalath, D., Champati ray, P. K., Bajaj, K., Podali, S., and Bisht, M. P. S. Integration of satellite remote sensing and geophysical techniques (electrical resistivity tomography and ground penetrating radar) for landslide characterization at Kunjethi (Kalimath), Garhwal Himalaya, India. *Natural Hazards*, 97(3):1191–1208, July 2019. doi: 10.1007/s11069-019-03695-0.

Kasperski, J., Delacourt, C., Allemand, P., and Pothérat, P. Evolution of the Sedrun Landslide (Graubünden, Switzerland) with Ortho-Rectified Air Images. *Bulletin of Engineering Geology and the Environment*, 69(3):421–430, Aug. 2010. doi: 10.1007/s10064-010-0293-z.

Kechavarzi, C., Soga, K., de Battista, N., Pelecanos, L., Elshafie, M. Z. E. B., and Mair, R. J. *Distributed fibre optic strain sensing for monitoring civil infrastructure: a practical guide*. ICE Publishing, London, 2016.

Kiers, T., Schmelzbach, C., Maurer, H., Amann, F., and Robertsson, J. Imaging one of the largest Alpine slope instabilities with 3D seismic first-arrival traveltime tomography. *Journal of Applied Geophysics*, 247:106081, Apr. 2026. doi: 10.1016/j.jappgeo.2025.106081.

Kleinbrod, U., Burjánek, J., Hugentobler, M., Amann, F., and Fäh, D. A comparative study on seismic response of two unstable rock slopes within same tectonic setting but different activity level. *Geophysical Journal International*, 211(3):1428–1448, Dec. 2017. doi: 10.1093/gji/ggx376.

Kurashima, T., Horiguchi, T., Izumita, H., Furukawa, S.-i., and Koyamada, Y. Brillouin Optical-Fiber Time Domain Reflectometry. *IEICE Transactions on Communications*, E76-B(4): 382–390, Apr. 1993. https://globals.ieice.org/en_transactions/communications/10.1587/e76-b_4_382/#.

Lacroix, P., Handwerger, A. L., and Bièvre, G. Life and death of slow-moving landslides. *Nature Reviews Earth & Environment*, 1(8): 404–419, Aug. 2020. doi: 10.1038/s43017-020-0072-8.

Lanz, E., Maurer, H., and Green, A. G. Refraction tomography over a buried waste disposal site. *GEOPHYSICS*, 63(4):1414–1433, July 1998. doi: 10.1190/1.1444443.

Larose, E., Carrière, S., Voisin, C., Bottelin, P., Baillet, L., Guéguen, P., Walter, F., Jongmans, D., Guillier, B., Garambois, S., Gimbert, F., and Massey, C. Environmental seismology: What can we learn on earth surface processes with ambient noise? *Journal of Applied Geophysics*, 116:62–74, May 2015. doi: 10.1016/j.jappgeo.2015.02.001.

Le Breton, M., Bontemps, N., Guillemot, A., Baillet, L., and Larose, E. Landslide monitoring using seismic ambient noise correlation: challenges and applications. *Earth-Science Reviews*, 216: 103518, May 2021. doi: 10.1016/j.earscirev.2021.103518.

Lee, C.-C., Yang, C.-H., Liu, H.-C., Wen, K.-L., Wang, Z.-B., and Chen, Y.-J. A Study of the hydrogeological environment of the lishan landslide area using resistivity image profiling and borehole data. *Engineering Geology*, 98(3):115–125, May 2008. doi: 10.1016/j.enggeo.2008.01.012.

Li, Z. Recent advances in earthquake monitoring I: Ongoing revolution of seismic instrumentation. *Earthquake Science*, 34(2): 177–188, Apr. 2021. doi: 10.29382/eqs-2021-0011.

Lindsey, N. J. and Martin, E. R. Fiber-Optic Seismology. *Annual Review of Earth and Planetary Sciences*, 49(1):309–336, 2021. doi: 10.1146/annurev-earth-072420-065213.

Lu, P., Lalam, N., Badar, M., Liu, B., Chorpening, B. T., Buric, M. P., and Ohodnicki, P. R. Distributed optical fiber sensing: Review and perspective. *Applied Physics Reviews*, 6(4):041302, Dec. 2019. doi: 10.1063/1.5113955.

Mainsant, G., Larose, E., Brönnimann, C., Jongmans, D., Michoud, C., and Jaboyedoff, M. Ambient seismic noise monitoring of a clay landslide: Toward failure prediction. *Journal of Geophysical Research: Earth Surface*, 117(F1), 2012. doi: 10.1029/2011JF002159.

Malehmir, A., Bastani, M., Krawczyk, C. M., Gurk, M., Ismail, N., Polom, U., and Perss, L. Geophysical assessment and geotechnical investigation of quick-clay landslides – a Swedish case study. *Near Surface Geophysics*, 11(3):341–352, June 2013. doi: 10.3997/1873-0604.2013010.

Malet, J.-P., Bertrand, C., Hibert, C., Radiguet, M., Lebourg, T., Gau-

tier, S., Bièvre, G., Vidal, M., Wanner, X., Lissak, C., et al. The OMIV service: acquiring and sharing long-period instrumental time series for documenting landslide activity. In *EGU General Assembly Conference Abstracts*, pages EGU–14542, 2023. doi: 10.5194/egusphere-egu23-14542.

Manning, T., Brooks, C., Ourabah, A., Popham, M., Ablyazina, D., Zhuzhel, V., Holst, E., and Goujon, N. The case for a nimble node, towards a new land seismic receiver system with unlimited channels. In *SEG Technical Program Expanded Abstracts 2018*, pages 21–25, Anaheim, California, Aug. 2018. Society of Exploration Geophysicists. doi: 10.1190/segam2018-2996250.1.

Masoudi, A. and Newson, T. P. Contributed Review: Distributed optical fibre dynamic strain sensing. *Review of Scientific Instruments*, 87(1):011501, Jan. 2016. doi: 10.1063/1.4939482.

Minardo, A., Damiano, E., Olivares, L., Picarelli, L., Zeni, L., Avolio, B., and Coscetta, A. Soil slope monitoring by use of a Brillouin distributed sensor. In *2015 Fotonica AEIT Italian Conference on Photonics Technologies*, pages 1–4, May 2015. doi: 10.1049/cp.2015.0156.

O'toole, T. B., Tranter, N., Hudson, T., Davidson, K., Dunham, C. K., Kiers, T., and Schmelzbach, C. A Review of Some Recent Large-N Nodal Seismic Experiments in Europe. In *AGU Fall Meeting Abstracts*, volume 2024, pages S52B–04, 2024.

Ouellet, S. M., Dettmer, J., Lato, M. J., Cole, S., Hutchinson, D. J., Karrenbach, M., Dashwood, B., Chambers, J. E., and Crickmore, R. Previously hidden landslide processes revealed using distributed acoustic sensing with nanostrain-rate sensitivity. *Nature Communications*, 15(1):6239, July 2024. doi: 10.1038/s41467-024-50604-6.

Paitz, P., Edme, P., Gräff, D., Walter, F., Doetsch, J., Chalari, A., Schmelzbach, C., and Fichtner, A. Empirical Investigations of the Instrument Response for Distributed Acoustic Sensing (DAS) across 17 Octaves. *Bulletin of the Seismological Society of America*, 111(1):1–10, Feb. 2021. doi: 10.1785/0120200185.

Patton, A. I., Rathburn, S. L., and Capps, D. M. Landslide response to climate change in permafrost regions. *Geomorphology*, 340: 116–128, 2019. doi: 10.1016/j.geomorph.2019.04.029.

Perrone, A., Lapenna, V., and Piscitelli, S. Electrical resistivity tomography technique for landslide investigation: A review. *Earth-Science Reviews*, 135:65–82, Aug. 2014. doi: 10.1016/j.earscirev.2014.04.002.

Pertuz, T. and Malehmir, A. Ultrahigh-resolution 9C seismic survey in a landslide prone area in southwest of Sweden. *Geophysical Journal International*, 235(3):2094–2106, Dec. 2023. doi: 10.1093/gji/ggad346.

Poli, P. Creep and slip: Seismic precursors to the Nuugaatsiaq landslide (Greenland): Seismic Precursors to a Landslide. *Geophysical Research Letters*, 44(17):8832–8836, Sept. 2017. doi: 10.1002/2017GL075039.

Provost, F., Malet, J.-P., Hibert, C., Helmstetter, A., Radiguet, M., Amitrano, D., Langet, N., Larose, E., Abancó, C., Hürlimann, M., Lebourg, T., Levy, C., Le Roy, G., Ulrich, P., Vidal, M., and Vial, B. Towards a standard typology of endogenous landslide seismic sources. *Earth Surface Dynamics*, 6(4):1059–1088, Nov. 2018. doi: 10.5194/esurf-6-1059-2018.

Rodríguez Tribaldos, V. and Ajo-Franklin, J. B. Aquifer Monitoring Using Ambient Seismic Noise Recorded With Distributed Acoustic Sensing (DAS) Deployed on Dark Fiber. *Journal of Geophysical Research: Solid Earth*, 126(4), Apr. 2021. doi: 10.1029/2020JB021004.

Rossi, G., Nocentini, M., Lombardi, L., Vannocci, P., Tanteri, L., Dotta, G., Bicocchi, G., Scaduto, G., Salvatici, T., Tofani, V., Moretti, S., and Casagli, N. Integration of multicopter drone measurements and ground-based data for landslide monitor-

ing. In *Landslides and Engineered Slopes. Experience, Theory and Practice*, pages 1745–1750. CRC Press, 2016. Num Pages: 6.

Samyn, K., Travelletti, J., Bitri, A., Grandjean, G., and Malet, J.-P. Characterization of a landslide geometry using 3D seismic refraction traveltime tomography: The La Valette landslide case history. *Journal of Applied Geophysics*, 86:120–132, Nov. 2012. doi: 10.1016/j.jappgeo.2012.07.014.

Schenato, L., Palmieri, L., Camporese, M., Bersan, S., Cola, S., Pasuto, A., Galtarossa, A., Salandin, P., and Simonini, P. Distributed optical fibre sensing for early detection of shallow landslides triggering. *Scientific Reports*, 7(1):14686, Oct. 2017. doi: 10.1038/s41598-017-12610-1.

Schöpa, A., Chao, W.-A., Lipovsky, B. P., Hovius, N., White, R. S., Green, R. G., and Turowski, J. M. Dynamics of the Askja caldera July 2014 landslide, Iceland, from seismic signal analysis: precursor, motion and aftermath. *Earth Surface Dynamics*, 6(2): 467–485, June 2018. doi: 10.5194/esurf-6-467-2018.

Senfaute, G., Duperret, A., and Lawrence, J. A. Micro-seismic precursory cracks prior to rock-fall on coastal chalk cliffs: a case study at Mesnil-Val, Normandie, NW France. *Natural Hazards and Earth System Sciences*, 9(5):1625–1641, Oct. 2009. doi: 10.5194/nhess-9-1625-2009.

Sens-Schönfelder, C. and Wegler, U. Passive Image Interferometry and Seasonal Variations of Seismic Velocities at Merapi Volcano, Indonesia. *Geophysical Research Letters*, 33(21), 2006. doi: 10.1029/2006GL027797.

Shapiro, N. M. and Campillo, M. Emergence of broadband Rayleigh waves from correlations of the ambient seismic noise. *Geophysical Research Letters*, 31(7), 2004. doi: 10.1029/2004GL019491.

Shen, N., Chen, L., Wang, L., Hu, H., Lu, X., Qian, C., Liu, J., Jin, S., and Chen, R. Short-Term Landslide Displacement Detection Based on GNSS Real-Time Kinematic Positioning. *IEEE Transactions on Instrumentation and Measurement*, PP:1–1, Jan. 2021. doi: 10.1109/TIM.2021.3055278.

Sim, K. B., Lee, M. L., and Wong, S. Y. A review of landslide acceptable risk and tolerable risk. *Geoenvironmental Disasters*, 9(1):3, Jan. 2022. doi: 10.1186/s40677-022-00205-6.

Spillmann, T., Maurer, H., Green, A., Heincke, B., Willenberg, H., and Husen, S. Microseismic investigation of an unstable mountain slope in the Swiss Alps. *Journal of Geophysical Research: Solid Earth*, 112(7), 2007. doi: 10.1029/2006JB004723.

Tonnellier, A., Helmstetter, A., Malet, J.-P., Schmittbuhl, J., Corsini, A., and Joswig, M. Seismic monitoring of soft-rock landslides: the Super-Sauze and Valoria case studies. *Geophysical Journal International*, 193(3):1515–1536, June 2013. doi: 10.1093/gji/ggt039.

Uhlemann, S., Hagedorn, S., Dashwood, B., Maurer, H., Gunn, D., Dijkstra, T., and Chambers, J. Landslide characterization using P- and S-wave seismic refraction tomography — The importance of elastic moduli. *Journal of Applied Geophysics*, 134:64–76, Nov. 2016a. doi: 10.1016/j.jappgeo.2016.08.014.

Uhlemann, S., Smith, A., Chambers, J., Dixon, N., Dijkstra, T., Haslam, E., Meldrum, P., Merritt, A., Gunn, D., and Mackay, J. Assessment of ground-based monitoring techniques applied to landslide investigations. *Geomorphology*, 253:438–451, Jan. 2016b. doi: 10.1016/j.geomorph.2015.10.027.

Virieux, J. and Operto, S. An overview of full-waveform inversion in exploration geophysics. *GEOPHYSICS*, 74(6):WCC1–WCC26, Nov. 2009. doi: 10.1190/1.3238367.

Voisin, C., Garambois, S., Massey, C., and Brossier, R. Seismic noise monitoring of the water table in a deep-seated, slow-moving landslide. *Interpretation*, 4(3):SJ67–SJ76, Aug. 2016. doi: 10.1190/INT-2016-0010.1.

Wegler, U. and Sens-Schönfelder, C.   Fault zone monitoring with passive image interferometry. *Geophysical Journal International*, 168(3):1029–1033, Mar. 2007. doi: 10.1111/j.1365-246X.2006.03284.x.

Whiteley, J., Inauen, C., Wilkinson, P., Meldrum, P., Swift, R., Kuras, O., and Chambers, J. Assessing the risk of slope failure to highway infrastructure using automated time-lapse electrical resistivity tomography monitoring. *Transportation Geotechnics*, page 101129, Oct. 2023. doi: 10.1016/j.trgeo.2023.101129.

Whiteley, J. S., Chambers, J. E., Uhlemann, S., Wilkinson, P. B., and Kendall, J. M. Geophysical Monitoring of Moisture-Induced Landslides: A Review. *Reviews of Geophysics*, 57(1):106–145, 2019. doi: 10.1029/2018RG000603.

Zelt, C. A., Azaria, A., and Levander, A. 3D seismic refraction traveltime tomography at a groundwater contamination site. *GEOPHYSICS*, 71(5):H67–H78, Sept. 2006. doi: 10.1190/1.2258094.

Zhao, C. and Lu, Z. Remote Sensing of Landslides—A Review. *Remote Sensing*, 10(2):279, Feb. 2018. doi: 10.3390/rs10020279.

Łakomski, M., Guzowski, B., Plona, M., and Pęczek, K.   Determination of Brillouin Backscattering Strain and Temperature Coefficients in Telecommunication Optical Fibers. *International Journal of Electronics and Telecommunication*, 71(1): 203–208, Mar. 2025. https://ijet.ise.pw.edu.pl/index.php/ijet/article/view/10.24425-ijet.2025.153563.